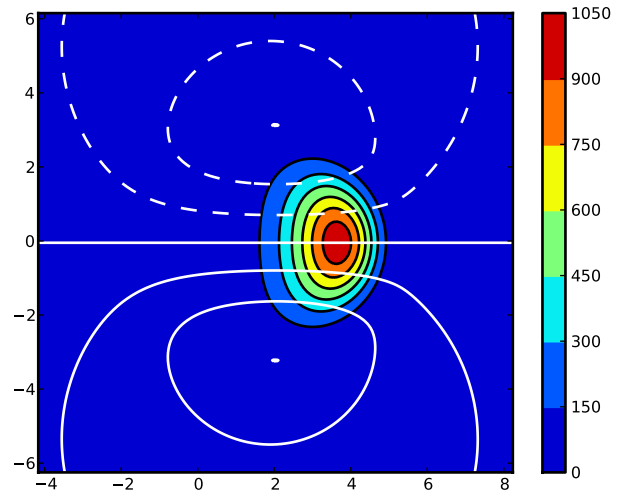
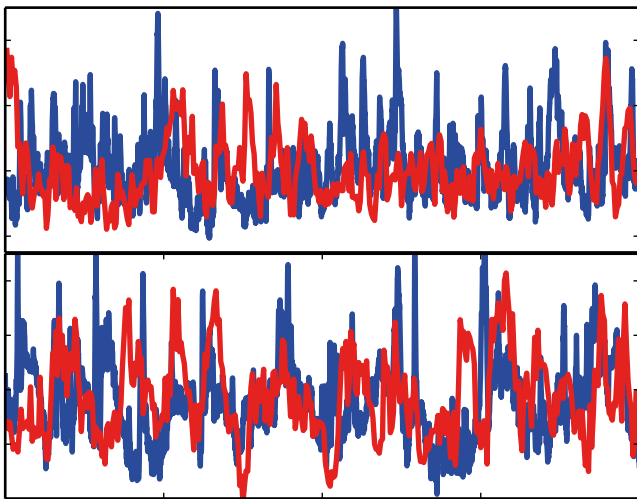
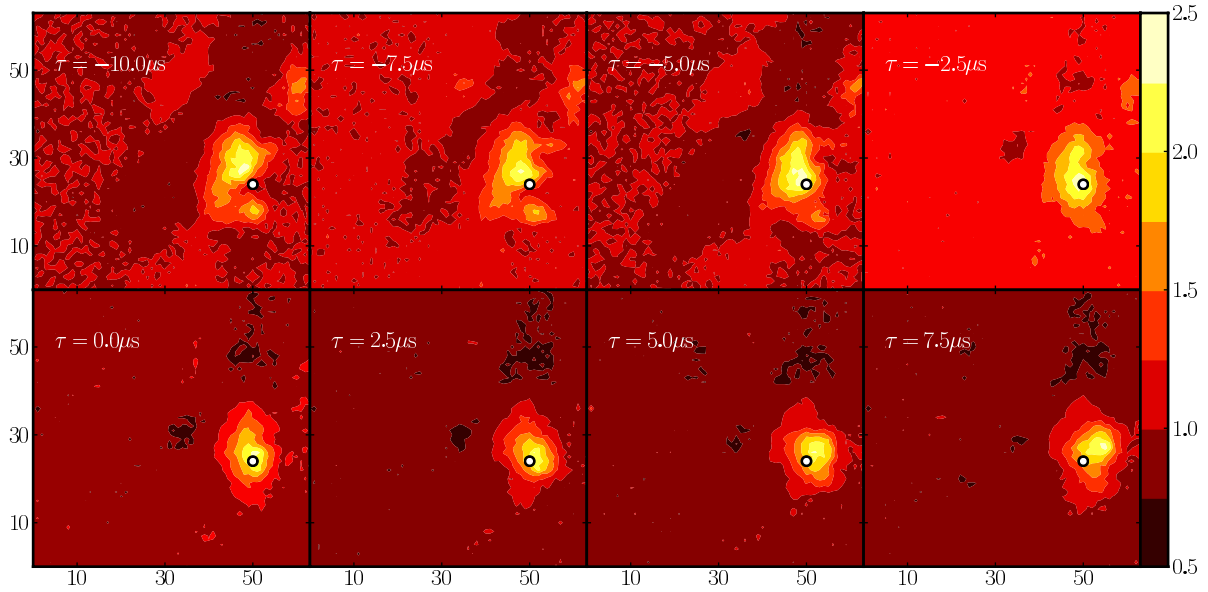


# Dynamics and statistical properties of blob structures in scrape-off layer plasmas

**Ralph Kube**

*A dissertation for the degree of Philosophiae Doctor – October 2014*



# Dynamics and statistical properties of blob structures in scrape-off layer plasmas

Ralph Arthur Kube\*

(Dated: October 16, 2014)

## Abstract

The velocity scaling of blobs, subject to dissipation by either electric currents to the sheaths, or dynamical friction, is studied by numerical simulations where the blob amplitude relative to the background plasma is a free parameter. When subject to dissipation by sheath currents, the radial velocity of a blob depends on the square of its cross field size  $\ell$ ,  $v_{\text{rad}} \sim \sqrt{\ell}$  for small  $\ell$ . For large  $\ell$ , the radial velocity of the blob scales as  $v_{\text{rad}} \sim \ell^{-2}$ . The radial blob velocity is maximal for an intermediate size and depends sensitively on the blob amplitude relative to the background density. In the case of dynamical friction, the blob velocity depends on its cross field size as  $v_{\text{rad}} \sim \sqrt{\ell}$  when friction is negligible. For strong friction the blob velocity is inversely proportional to the friction coefficient and size independent. The length scale for the transition between these velocity regimes depends sensitively on the relative blob amplitude.

An algorithm to track plasma blobs in spatially resolved optical measurements is developed and applied to gas-puff imaging data obtained from the scrape-off layer of the Alcator C-Mod tokamak. For discharges where the line averaged plasma density is small relative to the Greenwald density,  $\bar{n}_e/n_G \lesssim 0.3$ , the observed radial blob velocities are well approximated by the sheath connected velocity scaling. In the case of  $\bar{n}_e/n_G \gtrsim 0.4$ , the radial blob velocities are found to be larger than predictions by the sheath connected velocity scaling.

Statistical properties of the scrape-off layer plasma in Alcator C-Mod are studied for a series of discharges where the line-averaged particle density was varied. Long time series of the ion saturation current and the floating potential are obtained from Langmuir probes dwelled in the outboard mid-plane scrape-off layer as well as from a set of Langmuir probes embedded in the lower divertor baffle. We find that the waiting times between burst events and the burst amplitudes are approximately exponentially distributed. The exponentially distributed burst waiting times are compatible with the assumption that the individual blob events are uncorrelated. The conditionally averaged burst shapes of the saturation current perturbations and floating potential are similar for both poloidal positions at low line-averaged particle densities. For a discharge with high line-averaged density we find that the electric potential, sampled at the divertor, loses coherence with increasing distance to the last closed flux surface. These results indicate that sheath dissipation is a robust mechanism that governs the dynamics of plasma blobs in Alcator C-Mod at low line-averaged particle densities, while at high densities the blob filaments are electrically disconnect from the sheaths.

## CONTENTS

I. Plasma Blobs in Scrape-off Layer Plasmas	6
A. Nuclear Fusion in Magnetically Confined Plasmas	6
B. The Scrape-off Layer of Magnetically Confined Plasmas	11
C. The Road to Plasma Blobs	20
1. Theoretical Approach and Numerical Simulations	23
2. Single-Point Measurements	27
3. Gas Puff Imaging	31
4. Blob Generation Mechanism and Rate	34
II. Reduced Fluid Models for Magnetized Plasmas	36
A. Fluid Modeling	36
B. Reduced Fluid Model for Blob Simulations	38
1. Sheath Dissipation	43
III. Paper 1: Velocity Scaling for Filament Motion in Scrape-Off Layer Plasmas	46
IV. Paper 2: Interchange Motion of Large Amplitude Plasma Filaments	55
V. Paper 3: Blob sizes and velocities in the Alcator C-Mod scrape-off layer	64
VI. Paper 4: Convergence of statistical moments of particle density time series in scrape-off layer plasmas	69
A. Introduction	70
B. Stochastic Model	72
C. Statistical Estimators for the Gamma Distribution	75
D. Comparison to Synthetic Time Series	80
E. Discussions and Conclusion	82
F. Derivation of Mean-Squared Error on the Variance	84
VII. Paper 5: Fluctuation statistics in the scrape-off layer of Alcator C-Mod	97
A. Introduction	98
B. Fluctuation Statistics	101
C. Experimental Setup	103

D. Scrape-off Layer Statistics	105
E. Divertor Plasma Fluctuations	111
F. Discussion and Conclusions	114
G. Acknowledgements	118
VIII. Summary, conclusions and outlook	132
A. Summary and Conclusions	132
A. Simple toroidal coordinates	138
Acknowledgments	137
References	141

## I. PLASMA BLOBS IN SCRAPE-OFF LAYER PLASMAS

This thesis presents a study of the dynamics and statistical properties of blob structures in scrape-off layer plasmas. The scrape-off layer is the outermost shell of a plasma magnetically confined in toroidal geometry, as one might use to sustain nuclear fusion reactions and blobs are a mode, by which particles and heat are transported through this layer.

In order to discuss plasma blobs, we first introduce the concept of a magnetically confined plasma and motivate why they are useful to sustain controlled thermonuclear fusion reactions.

### A. Nuclear Fusion in Magnetically Confined Plasmas

Consider two light nuclei. For example deuterium, composed of one proton and one neutron, and tritium, composed of one proton and two neutrons. The constituents of these two nuclei can be rearranged into one Helium nucleus, consisting of two protons and two neutrons, and one excess neutron. The number of nucleons is conserved in this process, but the products weigh 17.6 MeV less than the reactants. Accounting for this, the reaction can be written as



The difference in mass is converted into kinetic energy of the neutron, 14.1 MeV, and of the Helium nucleus, 3.5 MeV. This is an example of a nuclear fusion reaction and the basis of the attempt to utilize nuclear fusion as a clean energy source with abundant fuel. It is also one of the many fusion processes that power the sun and other stars. Sustaining nuclear fusion reactions requires an environment of immense temperature, more than  $10^8$  K for the fusion reaction described by Eqn. (1). The sun sustains such conditions by its intense pressure owed to its mass. On earth, fusion reactions can be sustained by confining a sufficiently hot plasma using magnetic fields. For a strong enough magnetic field, the plasma particles gyrate around the field lines while streaming freely along the field lines. To avoid end losses of plasma, configurations where the magnetic field lines are closed are preferred.

The tokamak is just such a concept. It was invented in the Soviet Union in the 1950s and generates magnetic field lines that lie on a set of nested toroidal surfaces, as illustrated in

Fig. 1. These toroidal surfaces have the same shape as a tire, or a donut. Mathematically, a toroidal surface can be defined as the rotational surface of a circle around a co planar axis. In addition to the structures shown in Fig. 1, tokamaks feature a vessel wall that encompasses the confined plasma.

Before we discuss the properties of toroidally confined plasmas further, we introduce simple toroidal coordinates as described by Fig. 2. Denoting Cartesian coordinates by  $\mathbf{x} = (x, y, z)$  with an origin centered to the torus, the vertical symmetry axis of the torus is given by the  $y$ -axis. The distance between this symmetry axis and the center of the circle used to generate the toroidal surface is  $R_0$ , the major radius. Simple toroidal coordinates  $(r, \theta, \zeta)$  are defined by the transformation

$$r = \sqrt{y^2 + u^2} \quad \theta = \tan^{-1} \left( \frac{y}{u} \right) \quad \zeta = \tan^{-1} \left( \frac{z}{x} \right),$$

where  $u = \sqrt{x^2 + z^2} - R_0$  is the distance to the symmetry axis in the  $x$ - $z$ -plane. The total distance of from point to the symmetry axis is given by  $R = R_0 + r \cos \theta$ . The angle  $\theta$  is the so-called poloidal angle and gives the angle to the horizontal plane. This is the short way around the torus. The direction along the angle  $\zeta$  is the toroidal direction, the long way around the torus. The direction along  $r$  is the radial direction. The intersection between the coordinate axis  $r$  and the vessel wall of a tokamak is called the minor radius,  $a$ . Most tokamaks feature  $a \ll R_0$ . For example, the Alcator C-Mod tokamak [1] has  $a/R_0 \approx 0.32$ .

The electric current in toroidal field coils induce a toroidal magnetic field and a central transformer induces an electric current in the plasma. In turn, this generates a poloidal magnetic field. The resulting magnetic field lines intersperse a toroidal volume, winding along helical paths on a set of nested toroidal surfaces. Each of these nested tori confines a fraction of the plasma. This allows a smooth plasma pressure gradient, orientated perpendicular to the magnetic surfaces [2]. Auxiliary poloidal field coils superpose another vertical component of the magnetic field for confinement stability as well as for plasma positioning and shaping. This magnetic field geometry is the most promising route for plasma confinement and controlled nuclear fusion.

The magnetic field exerts a force against the kinematic pressure of the plasma that acts such as to expand the volume occupied by the plasma. Since the plasma occupies a toroidal volume, its surface area on the outwards facing half-torus is larger than its surface area of the inwards facing half-torus. This produces a net force that pushes the entire plasma column

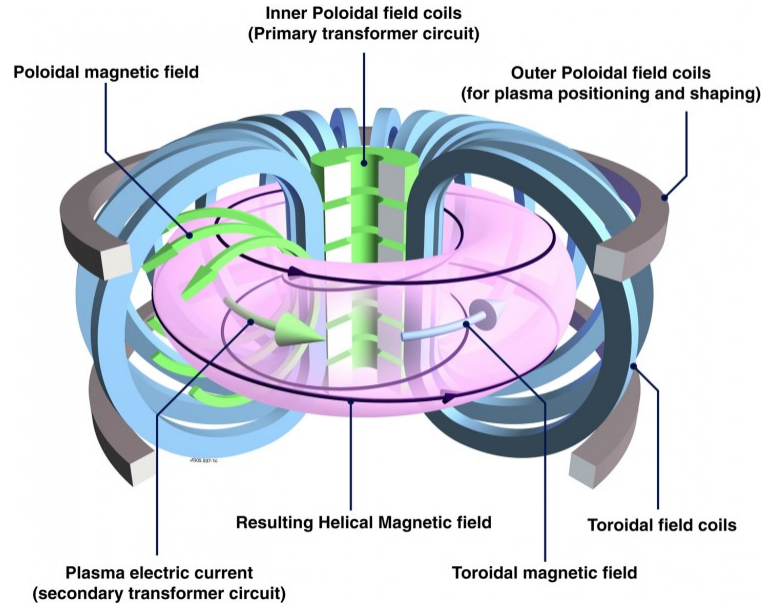


FIG. 1. The tokamak concept for magnetic confinement. The toroidal field coils create a toroidal magnetic field (blue color). The central solenoid induces an electric current in the toroidal direction, which generates the poloidal magnetic field (green color). The resulting helical magnetic field (black lines) confines the plasma. Source: <http://www.efda.org>

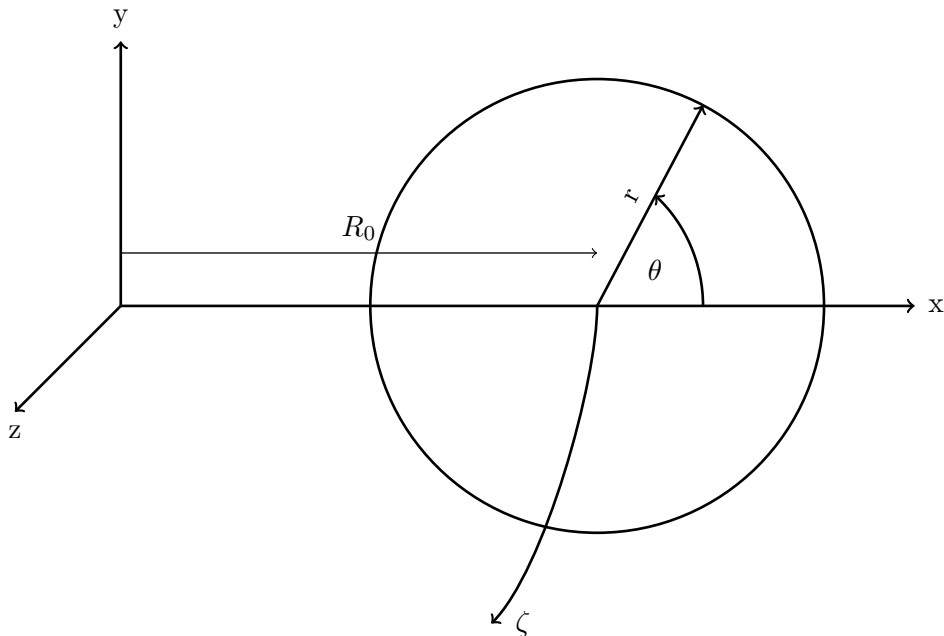


FIG. 2. Simple toroidal coordinates. The direction along the angular coordinate  $\theta$  is called the poloidal direction and the direction along  $\zeta$  is called the toroidal direction. The distance to the vertical symmetry axis  $R_0$  is the major radius.

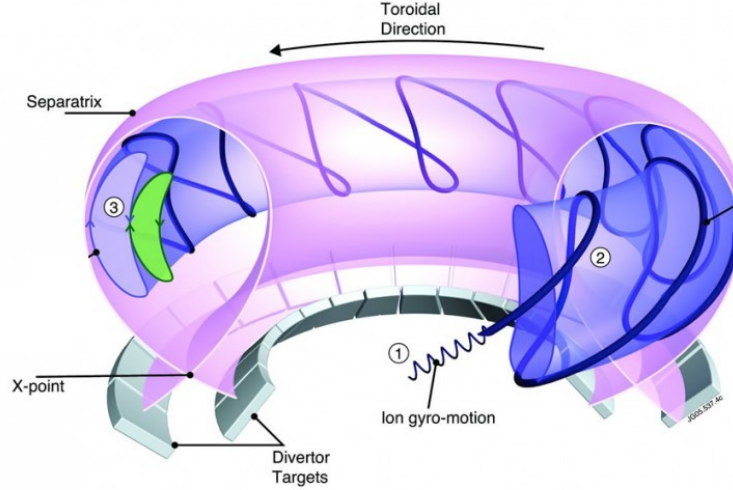


FIG. 3. In a diverted tokamak, the magnetic field is shaped as to divert the designated area of interaction between the plasma and the material wall away from the main plasma. Source: <http://www.efda.org>

radially outwards [3]. Furthermore, the toroidal component of the magnetic field is inversely proportional to  $R$ . It can be shown that this also results in a net force, acting such as to push the plasma column radially outwards [3]. To remedy these two forces, one commonly applies a homogeneous vertical magnetic field to the plasma. The resulting magnetic field impedes the outward expansion force of the plasma as to balance it in an equilibrium.

On the other hand, a plasma cannot be confined by a purely toroidal magnetic field. The magnetic curvature and gradient drifts of the particles result in a vertical electric polarization of the plasma column. As a result, the entire plasma column moves radially outwards. As shown in Fig. 3, superposing a poloidal field on the toroidal magnetic field inhibits this charge separation. As an ion drifts helically along the magnetic field in the toroidal direction, the poloidal component of the magnetic field guides it through several poloidal revolutions. Thus, the poloidal component of the magnetic field effectively shorts out the charge accumulation due to the drifts caused by the inhomogeneous toroidal field.

The magnetic field generated in a tokamak configuration necessarily extends throughout the volume enclosed by the vessel wall. When hot fusion plasma comes in contact with the wall, it may sputter atoms off the wall. These atoms may subsequently ionize and become impurities confined in the plasma. Commonly used wall materials are heavy metals,

such as Molybdenum or Tungsten, but also Carbon and Beryllium. Once ionized, impurities radiate Bremsstrahlung as they are accelerated in the plasma. This leads to radiative cooling, destabilizing the plasma confinement.

To improve plasma confinement it is therefore beneficial to restrict plasma wall interaction to an area remote from the main plasma. The divertor is just such a concept and is illustrated in Fig. 3. To divert the magnetic field such that it intersects material field lines underneath the plasma column, one may run an electric current, parallel to the toroidal plasma current, underneath the plasma column. The total poloidal component of the resulting magnetic field vanishes at one point, known as the X-point. As a consequence of the weak poloidal field in the region close to the X-point, the magnetic field lines spiraling downwards from the plasma column perform an increasing number of toroidal revolutions before striking the divertor targets [4]. This large magnetic connection length from the main plasma to the divertor targets allows the plasma to cool, predominantly by particle collisions and radiation, before striking the divertor targets [4 and 5].

The existence of the X-point divides the magnetic configuration into two distinct regions. Outside of the separatrix, the magnetic field lines intersect material walls. This region is called the scrape-off layer and is discussed in detail in the next section. Inside the separatrix, each of the nested tori may be classified as either a rational or an irrational surface. A irrational surface is defined by the trace of a non-closing magnetic field line. On the other hand, a toroidal surface may be traced out by magnetic field lines that close on themselves after performing  $m$  integral toroidal and  $n$  integral poloidal revolutions. Such surfaces are called rational surfaces. In the same way as a rational number  $m/n$  can be approximated by an irrational number, any rational surfaces can be approximated irrational surfaces and vice versa [6]. The mathematical existence of rational surfaces has significant consequences for the stability of a plasma. A linear stability analysis of the reduced magnetohydrodynamic equations reveals, that as a consequence of their existence, a singularity exists that allows the system to transition from a stable state into an unstable state [2]. This mechanism allows a wide range of instabilities, such as the sawtooth instability, which are observed experimentally.

The ratio  $m/n$  is also related to the safety factor  $q$ , which describes the pitch of the magnetic field lines. It can be approximated by the toroidal and poloidal component of the

magnetic field,  $B_T$  and  $B_P$ , as

$$q \approx \frac{r}{R_0} \frac{B_T}{B_P}. \quad (2)$$

A small value of  $q$  describes field lines that are wound into a tight helix while an infinitely large value of  $q$  describes a purely toroidal magnetic field [2]. The radial variation of  $q$ , called magnetic shear, can be controlled experimentally, and plays a significant role in the stability of plasma confinement [2 and 7]

## B. The Scrape-off Layer of Magnetically Confined Plasmas

The scrape-off layer of a magnetically confined plasma is its outermost region, encompassing plasma confined by closed magnetic surfaces. It is designed to remove the power exhausted by the confined plasma and may serve as a path for fusion ash removal in future fusion power plants. As plasma enters the scrape-off layer, it streams along the magnetic field towards the divertor targets. Under transient discharge conditions, the heat load on the divertor targets are readily of the order of  $\sim 100 \text{ MWm}^{-2}$  [8]. Handling heat fluxes of this magnitude is a major engineering problem for tokamak devices today and for future fusion power plants. It is therefore important to understand the transport processes that govern plasma transport in the scrape-off layer.

For a simple estimate of the scrape-off layer dimensions we use that for a magnetized plasma, subject to a laminar flow, the ratio between the parallel and perpendicular electron flux are ordered by the ratio of collision frequency to the gyro-frequency  $\Gamma_{\parallel}/\Gamma_{\perp} \approx (\nu_{e,i}/\Omega_{ce})^2 \ll 1$  [9]. Here,  $\nu_{e,i}$  is the electron ion collision frequency and  $\Omega_{ce}$  is the electron gyrofrequency. Assuming that there are no other momentum sources in the scrape-off layer,  $\nabla \cdot \mathbf{\Gamma} \approx 0$ , we find that  $\Gamma_{\parallel}/\Gamma_{\perp} \sim L_{\parallel}/L_{\perp} \ll 1$  [9]. Assuming that particles are lost at a constant rate along the direction perpendicular to  $\mathbf{B}$ , this results in an exponential decay of the parallel particle flux towards the divertor targets. It can be shown that this implies an exponentially decaying radial particle density profile [9]:

$$n_{\parallel}(\rho) = n_{\parallel}(0) \exp\left(-\frac{\rho}{\lambda_n}\right).$$

Here,  $\rho$  is a radial coordinate that measures the distance from the last closed flux surface as mapped to the outboard mid-plane by the magnetic field. This picture motivates the name

scrape-off layer. It is a region, where the plasma is scraped off from the main plasma to prevent a contact between the plasma and the main chamber wall. Typical length scales perpendicular to the magnetic field are  $L_{\perp} \sim 10^{-2}$  m, while the magnetic connection length in the scrape-off layer is  $L_{\parallel} \sim 10$  m. Thus, the volume of the scrape-off layer is small compared to the main plasma. Taking Alcator C-Mod with a major radius of  $R_0 = 0.67$  m and a minor radius of  $a = 0.22$  m as an example, the volume occupied by the scrape-off layer plasma is approximately 15% of the main plasma volume.

The picture presented above is highly simplified. Plasma in the scrape-off layer is in a turbulent state, characterized by order unity fluctuation amplitudes in the normalized electrostatic potential, electron temperature and electron density [10]. So far, no generally accepted model for the radial transport of particles and heat in scrape-off layer plasmas exists [11]. The parallel transport is also found to be sensitive to the parameters of the confined plasma. Furthermore, scrape-off layer plasmas are subject to complex interactions with neutral particles, due to their low temperature. Before discussing the properties of perpendicular and parallel transport in the scrape-off layer, we highlight the relevance of the scrape-off layer for plasma confinement.

Radial profiles of scrape-off layer plasma parameters, as measured by a reciprocating Langmuir probe in the *Tokamak á configuration Variable* (TCV), and Alcator C-Mod are shown in Figs. 4 and 5. In the case of a low line-averaged particle density  $\bar{n}_e$ , the radial particle density profile in Fig. 4 shows a two-region structure. Just outside of the last closed flux surface, the profile decays exponentially with a scale length of 5 mm. One centimeter inside the scrape-off layer, the profile decays exponentially with a scale length of 3 cm. The regions separated by the break point of the particle density profile are commonly referred to as near and far scrape-off layer. In the near scrape-off layer, next to the last-closed flux surface, one commonly observes a strong electric potential that is approximately given by the electron temperature,  $\phi \approx 3T_e$ , implying a poloidal shear flow due a radial gradient of the electric potential [9]. The far scrape-off layer presents nearly flat particle density and temperature profiles. This cold plasma may contribute to plasma recycling in the outboard mid-plane region as seen at Alcator C-Mod [12–15] and ASDEX Upgrade [16]. For a large line-averaged particle density, the particle density profile in the far scrape-off layer flattens out. The particle density profile presents only a single scale length, approximately 5 cm in the upper panel of Fig. 4. It lacks the separation into a near and far scrape-off layer, as was

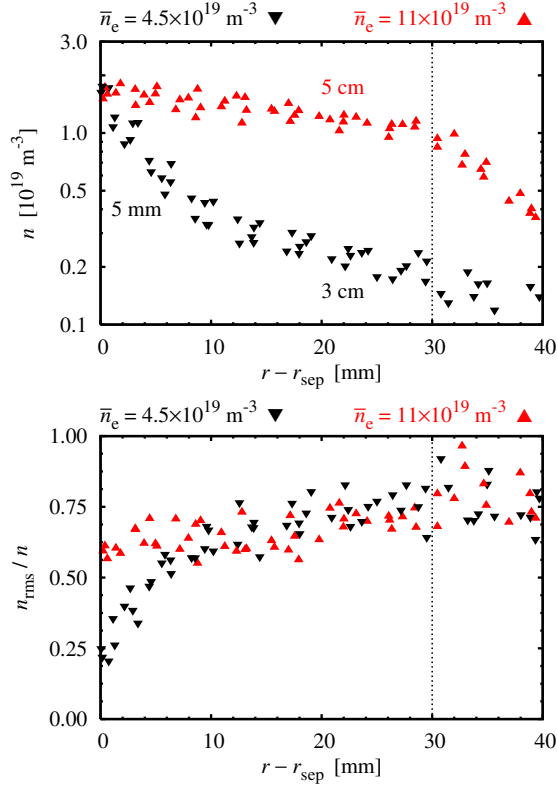


FIG. 4. Radial particle density profile (upper panel) and relative density fluctuation profile measured in the scrape-off layer of the TCV tokamak. Source: [17]

the case for a low line-averaged density. As shown in the lower panel of Fig. 4, the relative fluctuation level of the particle density is of order unity across the far scrape-off layer, and independent of the line-averaged plasma density. In terms of absolute fluctuation levels, the fluctuation amplitudes differ by a factor of five at the wall radius.

The particle density profiles in Fig. 5, panel(a), show the same two-region structure in Alcator C-Mod for  $\bar{n}_e/n_G = 0.19$ , where  $n_G$  is the Greenwald density. For a high line-averaged particle density,  $\bar{n}_e/n_G = 0.43$ , the particle density profile is nearly flat across the entire scrape-off layer, up to the limiter shadow. These profiles are taken from [18]. In these experiments it was observed that the radial particle transport, parameterized by an effective diffusion coefficient, increases with the line-averaged density. Furthermore, for a low line-averaged particle density, parallel heat conduction exceeds perpendicular heat convection in the near scrape-off layer and vice-versa in the far scrape-off layer. For a high line-averaged

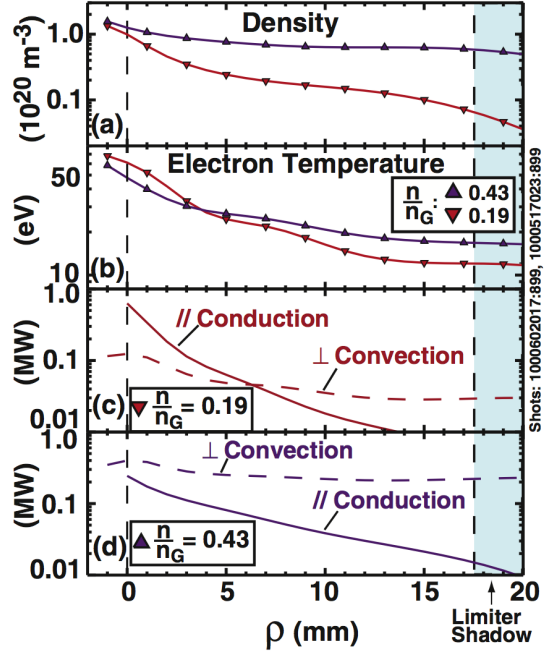


FIG. 5. Radial profiles of the electron density, electron temperature, and parallel, and perpendicular heat transport measured in the scrape-off layer of Alcator C-Mod. Source: [18], as reprinted in [19].

particle density, perpendicular heat convection exceeds parallel heat conduction by a factor of roughly 10 over the entire scrape-off layer, as shown in the two lower panel of Fig. 5. In the latter case, the observed particle density profile is also nearly flat, presenting no visible separation into a near and far scrape-off layer. It was argued that this cooling of the edge plasma, mediated by strong perpendicular heat convection, is linked to the empirical discharge limit observed in many toroidal confinement devices [18].

This connection between radial transport of heat in the scrape-off layer and the density limit was substantiated in [19] as follows. It was pointed out, that the parallel conductive heat transport scales as  $T_e^{7/2}$ , through  $\mathbf{q}_{\parallel,e} \sim \kappa_{\parallel}^e \nabla_{\parallel} T_e$ , where  $\mathbf{q}_{\parallel,e}$  is the parallel electron heat flux and  $\kappa_{\parallel,e}$  is the parallel electron heat conductivity. On the other hand, the perpendicular heat transport scales as  $T_e^{-3/2}$ , through the plasma collisionality  $\nu_{e,i}/\Omega_{ce}$ . This scaling of the parallel transport causes parallel heat flux to be self-regulating. Positive electron temperatures perturbations increase parallel heat conduction and oppositely for negative temperature perturbations. Both of these act as to impede the original temperature perturbation. Perpendicular heat transport on the other hand causes a positive feedback on the initial perturbation. A positive temperature perturbation leads to a decreased cross-field transport amplitude of the heat, thereby further increasing the temperature perturbation. A negative temperature perturbation leads to an increased cross-field transport amplitude of heat, decreasing the initial temperature perturbation further. As argued in [19], this allows negative temperature perturbations to move radially inward and may cause an onset of phenomena that are observed in density limit disruptions.

This establishes the importance of the scrape-off layer for plasma confinement in toroidal geometry. Since high plasma pressures are required to satisfy the Lawson criterion for plasma ignition,  $\langle p\tau_E \rangle \geq 8.3 \text{ atm s}$  for a plasma consisting of deuterium and tritium in equal numbers, sustaining high plasma pressures is a highly desirable property of any magnetic confinement configuration. We now proceed by giving a schematic description of the plasma transport from the confined plasma into the scrape-off layer.

Turbulence driven transport in the edge region, just inside the last closed flux surface, is commonly ballooned. It shows a peak amplitude at the outboard mid-plane region where the toroidal magnetic field is weakest. In other words, the region of large radial transport is poloidally localized. This ‘‘ballooning’’ character can be understood from the Shear-Alfvén law which describes the plasma vorticity dynamics in a model independent form. Starting

from the fluid momentum equation for a quasi-neutral plasma

$$\rho_m \frac{d\mathbf{V}}{dt} + \nabla \cdot \mathbf{\Pi} = -\nabla P + \mathbf{J} \times \mathbf{B},$$

where  $\rho_m$  is the plasma mass density,  $\mathbf{V}$  is the plasma center-of-mass velocity,  $\mathbf{\Pi}$  is the viscosity tensor, and  $\mathbf{J}$  is the electric current. We wish to express the plasma inertia by the curl of the velocity. The resulting equation gives the so-called Shear-Alfvén law [2]

$$\mathbf{B} \cdot (\nabla \times \mathbf{f} - 2\boldsymbol{\kappa} \times \mathbf{f}) = B^2 \mathbf{B} \cdot \nabla \left( \frac{J_{\parallel}}{B} \right) + 2\mathbf{B} \times \boldsymbol{\kappa} \cdot \nabla P. \quad (3)$$

Here,  $\mathbf{f}$  denotes the left hand side of the momentum equation, and  $\boldsymbol{\kappa} = \mathbf{b} \cdot \nabla \mathbf{b}$  is the magnetic curvature vector. Qualitatively, the Shear-Alfvén law relates the plasmas dynamics, expressed by the vorticity of the plasma inertia,  $\nabla \times \mathbf{f}$ , to driving forces on the right-hand side. These are expressed as parallel current driven modes, described by the first term on the right hand side, and as pressure gradient driven or interchange modes, described by the last term on the right hand side. A linear stability analysis reveals that in the case where  $\nabla P$  is parallel to  $\boldsymbol{\kappa}$ , interchange modes tend to be unstable [2]. This situation is referred to as unfavorable curvature. The region of unfavorable curvature in a toroidally confined plasma is just low field side region. Here, unstable interchange modes give rise to a poloidal asymmetry in the pressure fluctuations, which results in increased transport levels from the confined plasma into the outboard mid-plane scrape-off layer. This area is denoted by the outgoing wave fronts in Fig. 6.

The fluctuation amplitudes of the scrape-off layer plasma present a similar poloidal asymmetry. While the high field side scrape-off layer is usually in a quiescent state [20–25], relative fluctuation amplitudes of order unity in the electrostatic potential, electron temperature and electron density are regularly reported on the low field side scrape-off layer, accompanied by only modest fluctuations of the magnetic field [10]. Therefore, magnetic fluctuations are commonly neglected when modeling scrape-off layer plasma fluctuations. The quiescent regions of the scrape-off layer is denoted by QS, and the region where large amplitude fluctuations prevail is denoted by DW+IC in Fig. 6.

The connection between the high field side and the low field side scrape-off layer is accommodated by fluxes parallel to the magnetic field. These fluxes are denoted by the dashed arrows in Fig. 6 and commonly approach a velocity close to the acoustic speed  $C_s$ . They act such as to even out plasma pressure gradients within a magnetic flux tube and present rich

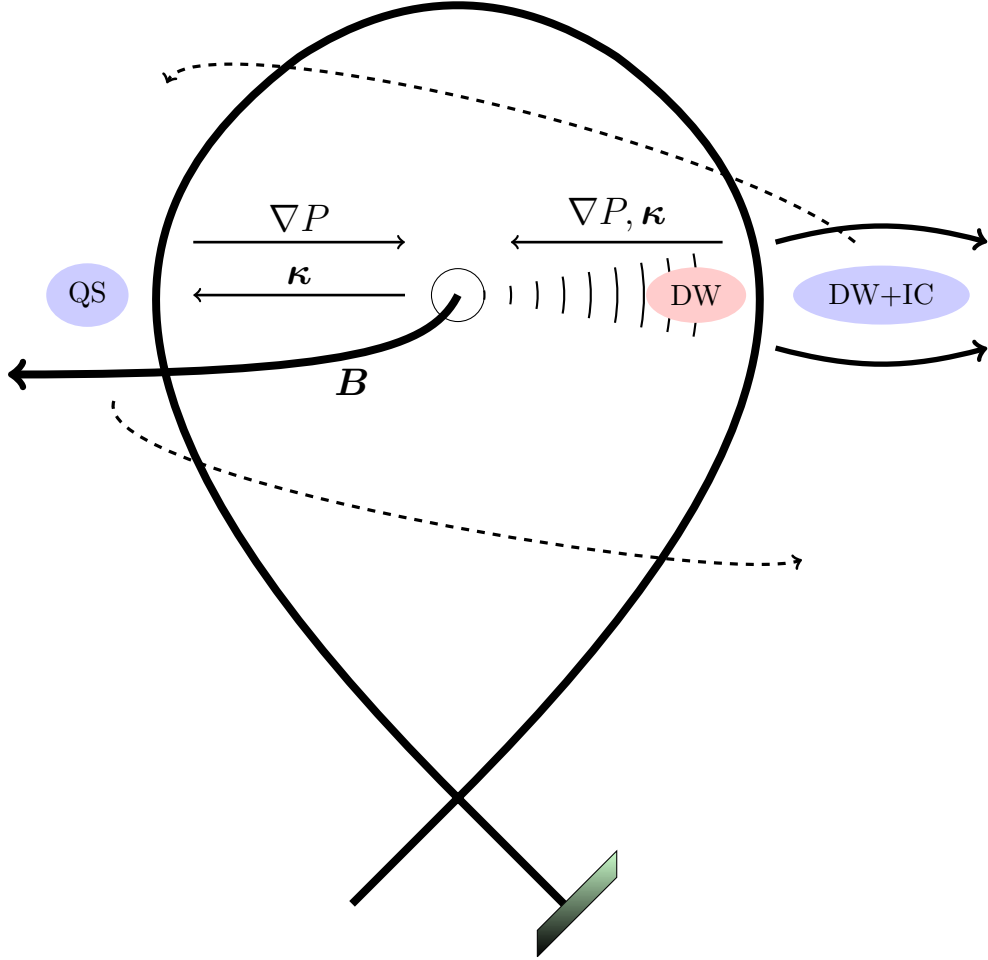


FIG. 6. A schematic of the various transport of plasma into the scrape-off layer and within the scrape-off layer. The region where the magnetic curvature is along the pressure gradient (denoted by the expanding wave) is poloidally localized and gives rise to elevated radial transport in the region denoted by DW. Plasma turbulence in this region has commonly drift wave (DW) character. As the plasma is transported into the scrape-off layer, parallel flows (dashed arrows) mediate plasma transport between the low field side scrape-off layer, where the observed turbulence features interchange (IC) like turbulence, as well as drift wave turbulence (IC+DW), and the quiescent high field side scrape-off layer (QS). In the region denoted by DW+IC one observes large radial fluxes towards the main chamber wall (denoted by the solid arrows pointing to the right).

dynamics as they are driven by a multitude of mechanisms. First, parallel Pfirsch-Schlüter flows arise a consequence of the toroidal geometry and their direction depends on the sign of  $B_T$  [26–28]. Parallel flows may also arise as a consequence of the ballooned transport

on the low field side. As strong radial transport at the low field side locally increases the static pressure of the plasma, the velocity of the parallel flows increases, thereby decreasing the dynamic pressure as to equilibrate pressure gradients along magnetic flux surfaces [21, 25, 28–30]. As a consequence, the dynamics of the quiescent high field side scrape-off layer is governed by near sonic parallel flows, which in turn are governed by the large fluctuation driven transport at the low field side scrape-off layer [21 and 25]. Experimental results [21, 25, 28–33] and numerical simulations [34 and 35] suggest that contributions from the mechanisms mentioned above indeed contribute significantly the observed parallel flows observed in scrape-off layer plasmas.

Having described the mechanism for plasma transport across the last closed flux surface into the scrape-off layer and along the magnetic field within the scrape-off layer, we now proceed to discuss the fundamental properties in which scrape-off layer turbulence differs from turbulence in the closed field line region.

The very design of the scrape-off layer distinguishes turbulence within the scrape-off layer qualitatively from turbulence within the closed magnetic field line regions [5]. First, perturbations without variation along the magnetic field are generally not allowed to exist in the closed field line region,  $\tilde{u}_{k_{\parallel}=0} = 0$ . Here, particle density and electric potential fluctuations are tightly coupled in their parallel dynamics, resulting in electrons that approximately follow a Boltzmann distribution along the magnetic field. This coupling is called adiabatic coupling and the fluctuations are drift wave turbulence. In contrast, the open field line geometry of the scrape-off layer allows fluctuations with a non-vanishing mean, i.e.,  $\tilde{u}_{k_{\parallel}=0} \neq 0$ , to exist [2].

Second, the interplay between heat transport along the magnetic field lines and the boundary conditions at the sheath, where the magnetic field lines intersect material walls, gives rise to a stationary radial electric field. This in turn generates a stationary poloidal electric drift [5 and 36].

The fact that perturbations with no variation along the magnetic field exist in the scrape-off layer relaxes the coupling between the particle density and electric potential fluctuations, dominant in the closed field line region. This may result in a damping mechanism acting on the electric potential, governed by the boundary conditions at the sheath entry [37–40]. The resulting turbulence has interchange character. A stationary radial electric field arises from the condition that the electric current entering the sheath vanishes when

averaged over time. This electric current is related to the ambient plasma via the sheath boundary condition:

$$J_{\text{se},\parallel} = -\mathbf{n} \cdot \mathbf{b} n_e e C_s \left\{ 1 - \exp \left[ \frac{e\phi(r)}{T_e(r)} \right] \right\}. \quad (4)$$

Here,  $\mathbf{n}$  and  $\mathbf{b}$  denote the unit vector of the material wall surrounded by the sheath, and the magnetic field respectively,  $\phi$  is the perturbation of the electric potential at the sheath entrance and  $T_e$  is the electron temperature [41]. Assuming perfect heat conduction along the magnetic field lines, the electron temperature and the electric potential profiles should be the same at the sheath entry. This profile, mapped along the magnetic field lines sets the stationary radial electric field in the scrape-off layer.

The case where the scrape-off layer plasma allows perfect heat conduction along the magnetic field is often referred to as the sheath-limited regime [5]. It describes the situation where the sheath determines the characteristics of the scrape-off layer. The regime, where large parallel temperature gradients in the scrape-off layer plasma exist is called the conduction limited regime. A temperature gradient may be supported by a finite parallel heat conductivity and the long magnetic connection length to the material walls. The divertor is just designed to support such a temperature drop. Experiments performed at the Alcator C-Mod tokamak suggest that the line-averaged plasma density serves as an experimental control parameter for this property of the scrape-off layer [42]. Here it was shown that for  $\bar{n}_e/n_G < 0.17$  scrape-off layer plasma is in the sheath-limited regime. The radial electron temperature profile at the outboard mid-plane scrape-off layer maps unchanged onto the divertor surface. The electrons in the divertor plasma are hot and the pressure along the magnetic flux tubes is constant. For  $0.17 < \bar{n}_e/n_G < 0.31$ , an electron temperature gradient along the magnetic field lines was observed, resulting in cold electrons in the divertor region. The particle density showed the opposite trend, such that no pressure gradient exists on the magnetic flux tubes. For  $\bar{n}_e/n_G > 0.31$ , the outermost region of the divertor, ca. 5 mm from the separatrix when mapped along the magnetic field to the outboard mid-plane, shows divertor detachment. Both, the divertor plasma density and the electron temperature were found to be significantly lower than the profiles at outboard mid-plane. This results in a electron pressure gradient along the magnetic field lines and in an increase of the neutral particle density in the divertor region.

We now have introduced mechanisms by which plasma is transported across the sep-

atrix into the scrape off layer. We have also discussed that plasma transport along the magnetic field depends on the line-averaged plasma density. We continue the discussion of the scrape-off layer by discussing plasma transport across the magnetic field.

So far, no model based on first principles that describes the observed cross-field transport in the scrape-off layer exists. It is common to model the time averaged cross-field particle flux as an effective diffusion: [15, 18, 43–46]

$$\langle \Gamma_{\perp} \rangle = -D_{\perp} \frac{\partial \langle n \rangle}{\partial r}.$$

Here,  $\partial/\partial r$  is the radial derivative, and  $D_{\perp}$  is a perpendicular diffusion coefficient. Experimental studies find that the magnitude of the estimated effective diffusion coefficient varies radially, sometimes over several order of magnitudes, in order to explain the observed particle density profiles [17, 18, 43, 44, and 46]. In [47] it was argued that it is not well founded to describe radial transport in scrape-off layer plasmas by either a diffusive process or by a convective velocity. For this, it was assumed that radial transport of a passive scalar  $\theta$  is described by  $\Gamma = -D\partial\theta/\partial r + V\theta$ , where  $D$  is a diffusion coefficient and  $V$  an effective velocity. A comparison of this model to particle fluxes calculated from interchange simulations [48–50] showed no obvious relation between the  $\Gamma$  and  $\nabla\theta$ . A similar result was obtained from experiments performed at the TCV tokamak [51]. Rather, a large body of research revealed that this anomalous transport is due to advective transport, mediated by the radial propagation of blobs.

After having outlined the fundamental properties which distinguish scrape-off layer turbulence from turbulence within the confined plasma, we now proceed to introduce the blobby transport paradigm. Even though the strongly turbulent nature of the scrape-off layer, which accompanied by order unity fluctuation levels of the particle density, has been known since the earliest experiments on magnetic plasma confinement in the 1960’s, these two properties were not merged into the blobby transport paradigm before the 2000’s. Motivated by this, we continue to review some main experimental results which coined the term “blob” and led to the establishment of the so-called blobby transport paradigm.

### C. The Road to Plasma Blobs

Plasma blobs are part of the complex phenomenology observed in the boundary layer of confined plasma in various confinement configurations. A recent review article by D’Ippolito et al. [52] recapitulates the large body of experimental and theoretical work over the last two decades on their properties. The term blob was coined as a description of coherent structures of excess particle density, localized in the plane perpendicular to the magnetic field, as observed by a two-dimensional array of Langmuir probes in the edge plasma of the Caltech tokamak [53]. This study showed however no evidence of preferred direction of motion, see Fig. 7, or correlation between their lifetime, amplitude, and propagation velocity.

In experiments, one universally observed large fluctuation amplitudes of the particle density, the electric potential, and the electron temperature, Fig. 8, while magnetic fluctuations were found to be negligible. Relative particle density and electric potential fluctuations of different magnitude were reported in [10], accompanied with a phase shift of approximately  $\pi/4 - \pi/2$ , suggesting that the electrons do not follow a Boltzmann relation [10]. The latter may be caused by collisions, electron inertia or plasma inductance.

Early theoretical work suggests that the observed large fluctuations in scrape-off layer plasmas are due to interchange modes which are unstable as a consequence of the sheath boundary conditions and unfavorable magnetic curvature [37 and 38]. The basis of the model used in these works is the so-called *flux gradient* paradigm, by which the growth rate of a mode is given by the scale length of the local plasma pressure.

Later experiments at the ASDEX device presented a detailed characterization of the electrostatic fluctuations in the scrape-off layer plasma [39]. Among others it was reported that the particle density fluctuations are elongated along the magnetic field and that the phase difference between peaks of the ion saturation current and floating potential signal are approximately  $\pi/2$ , see Fig. 9. It was also pointed out that a significant part of the radial transport due to electrostatic fluctuations was caused by few, large amplitude fluctuations. Guided by these observations, a mechanism was proposed by which electric drift eddies, elongated along the magnetic field, give rise to the observed large radial transport amplitudes, see Fig. 10.

Continuing research on large-amplitude particle density fluctuations in the scrape-off layer showed that they occur intermittently and linked the large-amplitude fluctuation

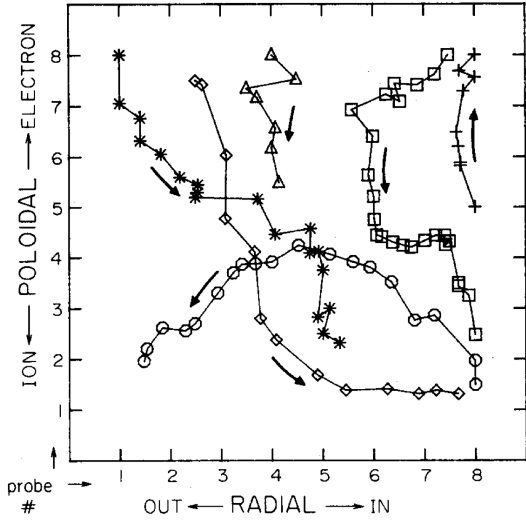


FIG. 7. Blob trajectories observed in the Caltech tokamak by Zweben et al. : [53]

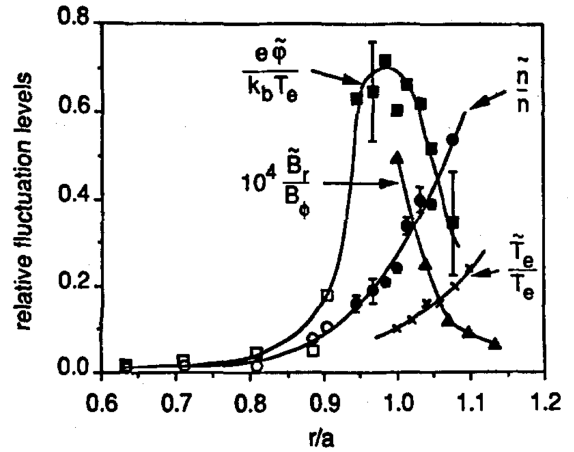


FIG. 8. Radial profile of the normalized rms fluctuation amplitudes of density  $\tilde{n}/n$ , potential  $e\tilde{\phi}/T_e$ , temperature  $\tilde{T}_e/T_e$  and magnetic field  $\tilde{b}_r/B_T$ . These values are measured in TEXT but characteristic for all tokamaks. Source: Wootton et al. [10]

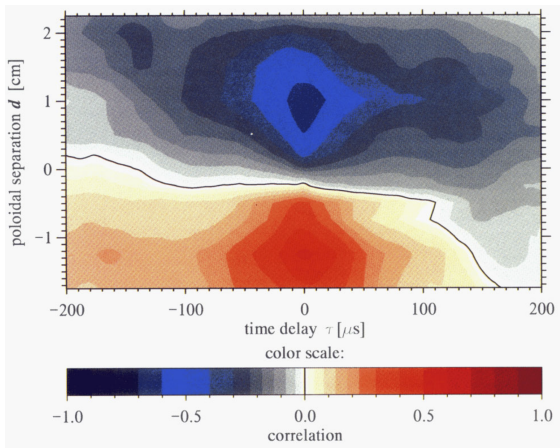


FIG. 9. “Cross-correlation between electric potential and ion saturation current” as observed in the ASDEX device by Endler et al. Source: [39]

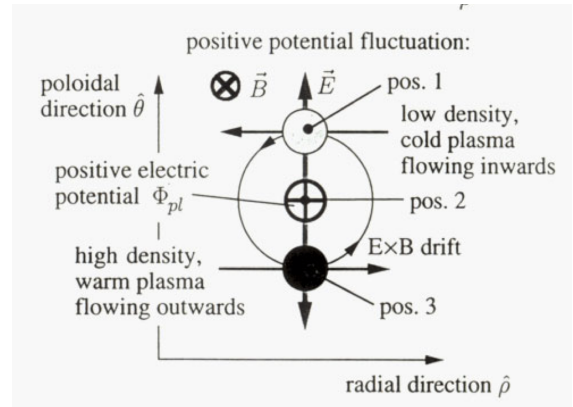


FIG. 10. “Eddy picture explaining the correlation between floating potential and ion saturation current”. Source: [39]

events to the radial propagation of coherent particle density structures that leave the confined plasma with a high radial velocity [54]. This work showed that “the radially propagating structures change the nature of the particle density fluctuations from random like fluctuations to bursty, intermittent fluctuations” [54], where the bursts present a characteristic asymmetric waveform, and that the coefficients of skewness and kurtosis of the sampled particle density fluctuations increase with distance to the last closed flux surface. It was pointed out that these features were qualitatively similar in two devices, suggesting that the observed radial plasma transport mediated by the radial propagation of coherent structures with large amplitude may be a universal mechanism in the boundary plasma [54]. The universality of this transport mechanism was subsequently substantiated by experiments on multiple tokamaks (DIII-D, Alcator C-Mod, MAST, Tore Supra, TCV) and linear devices (PISCES) [49, 55–59], which all presented similar features caused by the radial propagation of large amplitude plasma filaments in the scrape-off layer. This body of research established plasma blobs as a mechanism by which plasma and heat is transport ballistically out of the confined plasma.

This new paradigm directed the research on transport in scrape-off layer plasmas as to treat plasma blobs as self-contained objects and led to a plethora of experimental and theoretical work on plasma blobs [52]. Depending on the mode of observation, plasma blobs are commonly denoted as large amplitude burst events when recorded by single-point measurements and as blobs, when viewed in spatially resolved measurements perpendicular to the magnetic field. The term plasma filament is commonly used to refer to their full three dimensional structure.

Blobs are studied experimentally by three principle diagnostic setups [60]. First, single-point measurements are used to to compute statistical moments of the data time series, as the mean, the variance, skewness and excess kurtosis, and autocorrelation times. Statistical moments of time series are commonly used to describe the character of fluctuations in a turbulent flow field. Quantities pertaining to blobs as isolated events include conditionally averaged burst shapes [61] and their conditional variance [62], as well as statistics of the large amplitude burst events, for example the waiting times between subsequent events [63]. Second, two point measurements extend the methods available, by allowing to compute cross correlation functions for the two data time series. This includes cross correlation between density peaks and the electric potential [39, 64, and 65] as well as conditionally

averaged waveforms referenced to events of another waveform. Multi point observations from Langmuir probes arrays extend this method to a larger spatial domain. They are used predominantly in cold plasmas, as for example in TORPEX or VTF, and only infrequently in tokamaks. Finally, two-dimensional measurements, as for example gas-puff imaging, allow to compare fluctuation statistics over the total spatially resolved area. Analysis methods special to two-dimensional measurements include the reconstruction of the phase velocity flow field by time delay correlation techniques [66 and 67] and the reconstruction of three-wave coupling of the underlying turbulence by bicoherence analysis [68].

After having established the existence of plasma blobs and setting them in context with scrape-off layer turbulence, we now continue by discussing the methods used in the attached research papers, Sections III – VII . In the rest of this section, we discuss the basics of the reduced fluid model used Sections III and IV, and continue by discussing the principles of single-point measurements by Langmuir probes that is presented in Section VII. This is followed by an introduction to the gas-puff imaging diagnostic which has been utilized in Section V. We finish this section by setting the statistical analysis, presented in Section VII in context with studies of the blob generation mechanism and of blob birth.

### 1. *Theoretical Approach and Numerical Simulations*

A reduced fluid model, containing the essential blob physics, may be derived from the equations of particle and charge density conservation for a quasi-neutral plasma:

$$\frac{dn}{dt} = 0 \tag{5a}$$

$$\nabla \cdot \mathbf{J}_\perp = -\nabla \cdot \mathbf{J}_\parallel. \tag{5b}$$

Here,  $n$  is the plasma particle density and charge conservation is expressed by suppressing the build-up of space charges,  $\rho_{\text{ch}}$ , by  $\partial\rho_{\text{ch}}/\partial t = 0$ . The components of  $\mathbf{J}$  perpendicular and parallel to the magnetic field are given by  $\mathbf{J}_\perp = \mathbf{b} \times (\mathbf{J} \times \mathbf{b})$  and  $\mathbf{J}_\parallel = \mathbf{J} - \mathbf{J}_\perp$ , respectively. With  $n$  and  $\mathbf{J}$  described by a fluid model, Eqs. (5) have been used to derive a minimal model that contains the essential physics inherent to the radial propagation of plasma blobs as follows [49, 69–71]. The left hand side term of Eqn. (5b) includes the compression of the diamagnetic current and the polarization current. The latter describes the collective plasma motion expressed by the plasma vorticity, while the compression of the diamagnetic

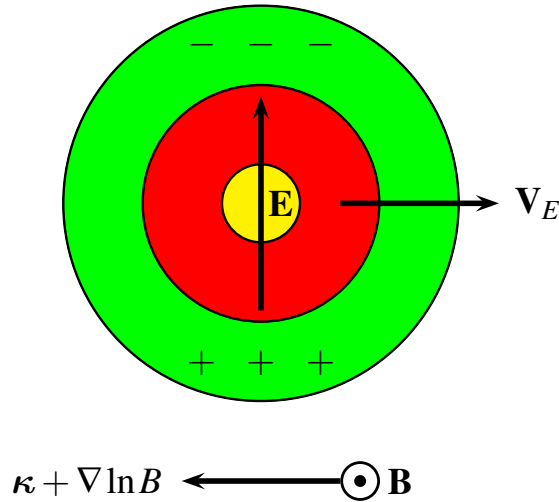


FIG. 11. At the outboard mid-plane, a patch of excess pressure is subject to interchange motions by which the structure is advected radially outwards. Source: [72].

current, which arises as a consequence of an inhomogeneous magnetic field and magnetic curvature, constitutes a source of vorticity. This can be understood when considering a patch of excess pressure at the outboard mid-plane, as illustrated in Fig. 11, and evaluating the Shear-Alfvén law, Eqn. (3) for this situation [49]. The structure has a pressure gradient that is perpendicular to both, magnetic curvature and gradient, such that  $\mathbf{B} \times \boldsymbol{\kappa}$  lies in the same plane as  $\nabla P$ . This constitutes a source of vorticity. Such motions, by which high density plasma is interchanged with low density plasma, are commonly called interchange motions. Adopting a particle picture, the magnetic gradient and curvature drift of charged particles is just such, as to polarize the structure in Fig. 11 vertically. This results in an electric drift by which the structure moves radially outwards by the electric drift [69].

If the blob is assumed to be unmodulated along the magnetic field, the compression of parallel current may be parameterized by the sheath boundary conditions Eqn. (4) [69]. In this limit, an analytical solution to Eqs. (5) for a blob of fixed shape propagating in a vacuum relates the blobs radial velocity to its cross-field size as  $v_{\text{rad}} \sim \ell^{-2}$ . This blob velocity scaling is commonly called the sheath limited velocity scaling [69].

Numerical simulations of such a reduced fluid model revealed that a seeded blob de-

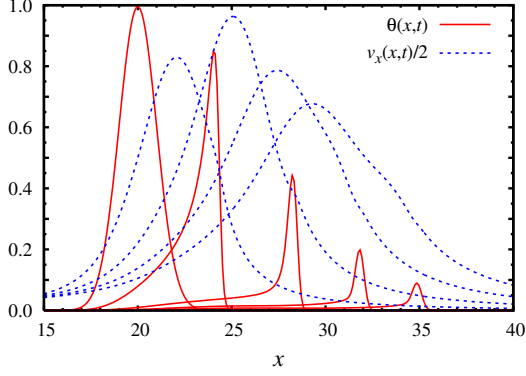


FIG. 12. Radial variation of the particle density (red line) and the radial velocity (blue dashed line) at the symmetry axis as observed by numerical simulations of seeded blobs [49 and 73]. The peaks correspond to increasing simulation time, starting from an initially resting structure given by the largest density peak. Source: [49].

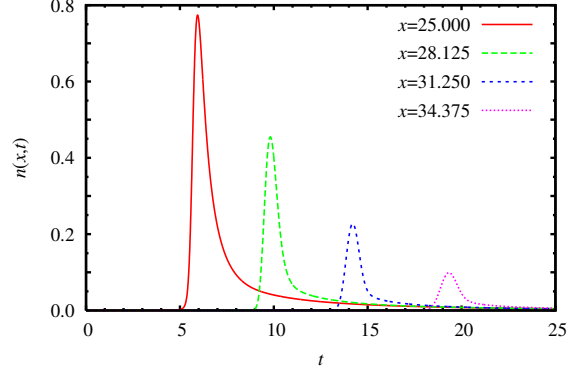


FIG. 13. Time series of the particle density, sampled at single points in a numerical simulation of a seeded blob, presented in [49]. The points are located at the symmetry axis of the simulation domain at radial positions as indicated by their  $x$  value. Initially the blob is at rest at  $x = 20.0$ . As it traverses the probe, the particle density wave form shows a steep front and a trailing wake for probes at  $x \leq 28.125$ . Source: [49]

velops a steep front and a trailing wake [49 and 73]. This blob was shown to evolve due to an electric drift, which transports plasma from the blobs front, around its lobes, into its wake. Fig. 12 shows the radial variation of particle density (red line) and radial velocity field (blue dashed line) at the symmetry axis observed in such a simulation [49]. The peaks correspond to increasing simulation time, starting from the initial condition given by the peak with largest amplitudes. This suggests that the flow field generated by the blob acts to generate the steep front and the trailing wake of the particle density field [73]. The evolution of the particle density measured at single points of such a simulation are shown in Fig. 13. The points where the density was sampled are located on the poloidal symmetry axis of the simulation domain at a radial coordinate  $x$ . Initially, the blob was at rest and centered at the point  $x = 20$ . As the blob traverses the points at  $x = 25.0$  and  $x = 28.125$ , the time series of the particle density present a steep front and a trailing wake. These features are less pronounced at the time series sampled at  $x > 28.125$ , as small scale flows decorrelate

the blob structure over its propagation.

An advantage of using reduced fluid models to study blob propagation is that they allow to eliminate physical processes which are believed to be unimportant for the dynamics. This may include field line fluttering due to the propagation of Alfvén waves along the magnetic field or sound waves. Furthermore, are they mathematically simplified. In the electrostatic approximation for example, one may express the cross-field dynamics by the scalar electrostatic potential. This reduces a vector equation, the fluid momentum equation, to a scalar equation, the vorticity equation.

It is the flexibility allowed by relating the parallel currents, the right hand side of Eqn. (5b), to a multitude of plasma parameters that allow a quick insight into blob dynamics within the regime at hand. Several closures for the electric current loop have been studied in the literature [74]. Among others, the dispersion of parallel currents in the region of an X-point [75–79], and electromagnetic effects due to outgoing Alfvén waves [80]. For high plasma collisionality, the electron motion along the magnetic field is strongly impeded, yielding  $\nabla \cdot \mathbf{J}_{\parallel} = 0$ . In this regime, often called the ideal, or hydrodynamic regime, the radial blob velocity scales as  $v_{\text{rad}} \sim \sqrt{\ell}$  [49 and 79].

The fact that closures for the compression of the parallel current do not change the nature of the dominant non-linearities of the model equations has been used to reveal the scaling of the radial blob velocity with its plasma parameters for several closures of the parallel current source. Employing dimensional analysis, one relates the linear growth rate of Eqs. (5) to the radial blob velocity and its cross-field size by estimating  $v_{\text{rad}} \sim \hat{\omega}\ell$  and  $k_{\perp} \sim 1/\ell$ , where  $\hat{\omega}$  is the growth rate of the most unstable linear mode and  $k_{\perp}$  is the wavenumber perpendicular to the magnetic field [78]. This method is called the “blob correspondence principle” and is commonly used to map blob velocity scaling regimes onto the parameter space of the underlying system of linearized equations. In order to relate the growth rate of the systems most unstable mode to the radial blob velocity, in the framework of the blob correspondence principle, it is assumed that the advective derivative and the time derivative of the inertial term are of the same order of magnitude,  $\partial/\partial t \sim \mathbf{V}_{\text{E}} \cdot \nabla$ , which suggests that the blob propagates as a static modulation on the background density. The blob correspondence principle has been used to derive blob velocity scaling regimes for several models, most prominently for models including closures relevant to X-point effects [78], two region models incorporating plasma collisionality and magnetic shear as free parameters [79],

and the DALF model with warm ions [81–84].

As the velocity scaling derived from the blob correspondence principle relies on the balance of vorticity sources and sinks it gives the boundaries of different blob velocity scaling regimes but cannot describe the transition from one regime to another. Papers 1 and 2 of this thesis describe the transition from the ideal regime to the sheath dissipative and the friction dominated velocity scaling regime. Experiments at the TORPEX device show that electric currents to the sheath affect the blob dynamics [85–87]. Furthermore, analysis of imaging data, obtained at the NSTX tokamak and ASDEX Upgrade, suggest that sheath dissipation may also be relevant for blob dynamics in scrape-off layer plasmas [79 and 88]. Experiments at VTF suggest that the radial dynamics of plasma blobs are influenced by the friction with neutrals. There it was found, that the radial velocity scaling of the plasma blobs is well described by the frictional velocity scaling regime  $v_{\text{rad}} \sim 1/\nu$  [89]. In tokamaks one frequently observes a high pressure of neutral gasses close to the vessel wall in the outboard mid-plane regions [12, 15, 90, and 91]. Here, collisional friction may also be relevant for blob dynamics [92].

## 2. *Single-Point Measurements*

Single-point measurements of the local plasma parameters are regularly performed using Langmuir probes. They allow to infer the local particle density and the plasma potential by measuring the electric current drawn by the probe when a voltage is applied to it. The relation between this current and voltage, and the local plasma parameters is described by Debye sheath theory, which describes the interaction between a material surface in contact with a plasma.

When any sufficiently cold material is inserted into a plasma, a thin layer will form around it. In the initial transient period where the cold surface is electrically neutral, electrons strike the surface at a higher rate than ions. As the electrons recombine with the surface, it assumes a negative charge. This impedes further electron flow towards the surface and results in a thin layer surrounding the surface in which ions shield the electric potential of the surface. This so-called sheath extends a few Debye lengths,  $\lambda_D = \sqrt{\epsilon_0 T_e / n_e e^2}$ , outwards from the surface into the plasma. It is a region characterized by a violation of quasi-neutrality,  $n_i > n_e$ , and by a strong electric field, as shown in Fig. 14. Here, the

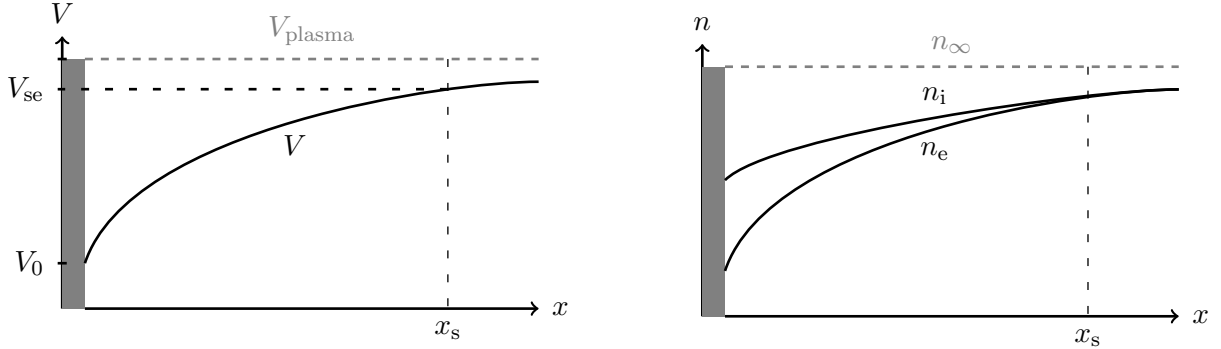


FIG. 14. Schematic of the electric potential and particle densities in the sheath formed at material surfaces

sheath extends from the material surface up to the point  $x_s$ , called the sheath entrance. Outwards from this point, only a small potential variations into the plasma. It can be shown that the electric potential at the sheath entrance, relative to the plasma potential, is given by  $V(x_s) \equiv V_s = -T_e/2e$  and that the particle density at the sheath entrance,  $n_{se} = n_e(x_s) \approx 0.61 n_e(x = \infty)$  [93], where  $n_e(x = \infty)$  is the local electron density of the plasma.

The electric current density drawn by a Langmuir probe is governed by the influx of electrons and ions at the sheath entrance. As shown in [93], the current also depends on the potential drop within the sheath region, and may be written as [41 and 93]

$$J_{pr}(\Delta V) = en_{se}C_s \left[ \exp\left(\frac{e\Delta V}{T_e} + \mu\right) - 1 \right], \quad (6)$$

where  $n_{se}$  is the particle density at the sheath entry,  $\Delta V = V_{plasma} - V(0) \approx V_{se} - V_0$  is approximately the potential drop within the sheath, and  $\mu = \ln \sqrt{m_i/2\pi m_e}$  is approximately 3 in a deuterium plasma. The first term in the parenthesis in Eqn. (6) is due to an electron flux towards the probe while the latter term is due to the ion flux. While the ion flux at the sheath entrance due the surface is given by  $n_{se}C_s$ , the electron flux towards the surface depends on the potential drop in the sheath.

In a steady state the current density drawn by the probe vanishes. The electric potential at any material surface assumes when it is not drawing current from the plasma is called the floating potential,  $V_{float}$ . Setting  $J_{pr} = 0$  then gives a relation between the floating

potential of the surface and the plasma potential,  $V_{\text{plasma}}$ :

$$V_{\text{plasma}} = V_{\text{float}} + 3\frac{T_e}{e}. \quad (7)$$

In the case of a constant electron temperature, the fluctuations of the floating potential are proportional to fluctuations of the plasma potential.

When the probe is biased to a large negative potential, almost all electrons entering the sheath are repelled by the Coulomb barrier given by the sheath electric potential. Consequently, only ions may pass through the sheath and the electric current drawn by the probe is only due to ions. In this case, Eqn. (6) reduces to

$$J_{\text{pr}}(V = -\infty) = en_{\text{se}}C_s \equiv J_{\text{sat}}, \quad (8)$$

where  $J_{\text{sat}}$  is the ion saturation current density. The ion saturation current measured by a probe with surface area  $A_{\text{pr}}$ ,  $I_{\text{sat}} = A_{\text{pr}}J_{\text{sat}} = en_{\text{se}}\sqrt{T_e/m_i}$  is proportional to the density at the sheath entry and proportional to square-root of the electron temperature. Fluctuations on the ion saturation current,

$$\tilde{I}_{\text{sat}} = en_e C_s \left( \frac{\tilde{n}}{n} + \frac{1}{2} \frac{\tilde{T}_e}{T_e} \right), \quad (9)$$

are governed by fluctuations in the particle density in the case where  $\tilde{n}/n \approx \tilde{T}_e/T_e$ . For the analysis of Langmuir probe data, presented in Paper 5, we assume just this.

The presented results from the Debye sheath theory are not only valid for Langmuir probes, but may apply to all cold material surfaces in contact with a plasma. Especially, Eqn. (6) may be used to derive the sheath boundary conditions, Eqn. (4), as shown in [41]. In this work Eqn. (4) was derived by a linearization of Eqn. (6) around the equilibrium  $J_{\text{pr}} = 0$ .

In the upper panel of Fig. 15, we present the normalized ion saturation current, as sampled from a Langmuir probe dwelling in the scrape-off layer of Alcator C-Mod. The time series presents intermittent, large amplitude burst events which exceed four times the standard deviation of the time series. Only few bursts with negative amplitude are observed. The lower panel shows the conditionally averaged waveform of large-amplitude events which exceed 2.5 times the standard deviation of the time series. Bursts used to compute this average are marked by a black dot in the upper panel. The conditionally averaged waveform is asymmetric, featuring a fast rise and a slow decay. These features are

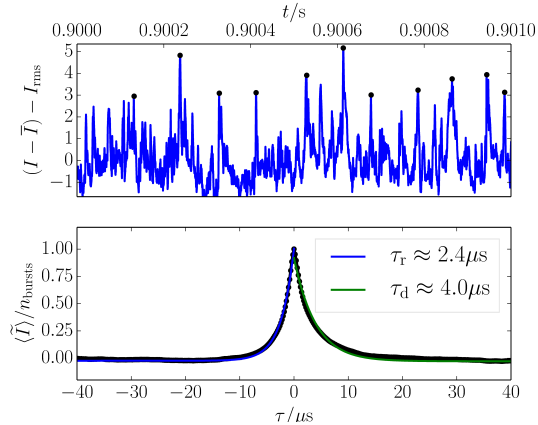


FIG. 15. Ion saturation current time series as sampled by a Langmuir probe in a scrape-off layer plasma (upper panel) and the conditionally averaged waveform of large amplitude bursts (lower panel). Exponential fits on the rise and decay time of the averaged waveform are denoted by respectively a blue and green line.

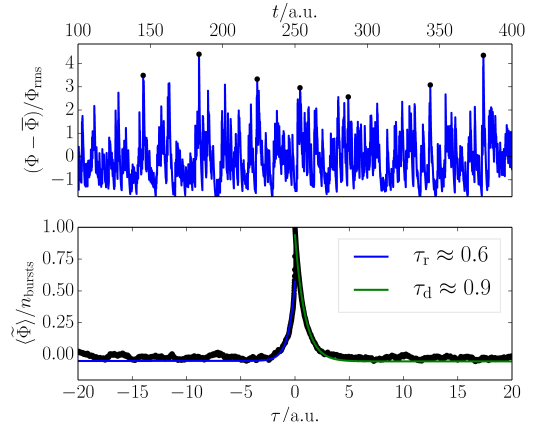


FIG. 16. Synthetic time series of the shot noise process described in [94] (upper panel) and the conditionally averaged waveform of large amplitude bursts (lower panel). Exponential fits on the rise and decay time of the averaged waveform are denoted by respectively a blue and green line.

attributed to the radial motion of plasma blobs. Exponential fits on the rise and decay of the averaged waveform yield  $\tau_r \approx 2.4 \mu\text{s}$  and  $\tau_d \approx 4.0 \mu\text{s}$  respectively. These fits are shown in a green and blue line in the figure. The realization of a particularly relevant stochastic process [94] is shown in the upper panel of Fig. 16. This process describes the observed time series as the superposition of pulses with a fixed, exponentially decaying pulse shape, with exponentially distributed pulse amplitudes and waiting times between pulses. The time series shows the same intermittent character as the time series sampled by the Langmuir probe. The conditionally averaged waveform of large-amplitude bursts also presents a fast rise and a slow decay, where  $\tau_r \approx 0.6$  and  $\tau_d \approx 0.9$ . Section VII of this thesis discusses the fluctuation statistics in the scrape-off layer plasma of Alcator C-Mod.

We conclude this subsection by noting a limitation of Langmuir probes which is the motivation for the work presented in Paper 4 of this thesis. Any Langmuir probe that is inserted in the edge region is subject to a large heat flux. This limits the region accessible by probes practically to the scrape-off layer, up to the last closed flux surface, as well as the time

a probe may be placed in this region. Commonly, Langmuir probes are reciprocated through the scrape-off layer. Thus, the duration where fluctuations within one spatial interval are sampled is short. Now, fluctuations are often characterized by statistics of the underlying data time series, as its mean, variance, skewness and kurtosis. In order to assess the error introduced by this finite sample length, expressions for the mean-squared error on the sample mean and variance were derived based on the stochastic model presented in [94]. As discussed in Section VII, this stochastic model is relevant to modeling the plasma fluctuations as observed by single point measurements.

### 3. *Gas Puff Imaging*

Gas puff imaging is an optical diagnostic, commonly employed to study the characteristics of a turbulent plasma in regions inaccessible to Langmuir probes. By recording emissions originating from within the confined plasma, gas puff imaging methods circumvent the limitations of Langmuir probes as to extend the region accessible to measurements some centimeters beyond the last closed flux surface as well as the duration of the data time series.

Due to the large temperatures of fusion relevant plasmas, the peak of their emitted light is not in the visible range. Furthermore, the emission source is diffuse and not located in space. Puffing a jet of contrast gas into the plasma induces light emissions from a well defined region of the plasma, which commonly exceed the intrinsic emissions of the plasma by a factor of approximately 5 for certain wavelengths [95]. Common contrast gasses used in Alcator C-Mod are Deuterium and Helium. Upon contact with the plasma, inelastic collisions excite the neutral gas atoms. When receding to their ground state, they emit light with frequencies determined by the structure of the atoms electron shell. These emissions are captured by a bundle of fiber optics installed in a periscope, which views the main chamber tangentially to the magnetic field. The optics commonly filter the light, as to pass only one wavelength. For Hydrogen this is the Balmer  $\alpha$  line, originating from the  $3n \rightarrow 2n$  transition, with a wavelength of  $\lambda = 656.1$  nm. For Helium, the wavelength filter passes light with a wavelength of  $\lambda = 587.6$  nm, originating from the  $3^3D \rightarrow 2^3P$  transition [68]. The filtered light is subsequently passed to a recording device, such as a fast charge coupled device (CCD) camera [96–98] or an array of avalanche photo diodes (APD) [68],

which samples the emission intensities spatially resolved. The intensity of the contrast gas emission  $I$  depends on the electron density  $n_e$ , the electron temperature  $T_e$ , the density of the contrast gas  $n_0$ , and the radiative decay rate for the transition passed through the filter  $A_{\text{rd}}$ , as

$$I = n_0 f(n_e, T_e) A_{\text{rd}}. \quad (10)$$

Here, the emissivity  $f$  models the dependence of the emission intensity on  $n_e$  and  $T_e$ . In this sense, “gas puff imaging measures the effect of the underlying plasma turbulence on the emissions” [95].

This leads to some specialties of this measurement technique. For one, the sampled intensity depends on the electron density and the electron temperature in a non global way. This is commonly modeled as  $f(n_e, T_e) \sim n_e^\alpha T_e^\beta$ , where  $\alpha$  and  $\beta$  depend on the background electron temperature and density [99]. For common scrape-off layer plasma parameters,  $\alpha \approx 5\beta$ , such that the measured intensity fluctuations are taken to be mostly due to particle density fluctuations [68]. Second, in order to be able to compare emission amplitudes from spatially separated points, the neutral particle density needs to assume similar values in these points [100]. Third, the influence of the neutral contrast gas on the plasma should not modify the plasma turbulence significantly. Empirical studies show that the frequency spectrum of ion saturation current time series as sampled by a Langmuir probe, resembles the frequency spectrum of emission intensity, as sampled by gas puff imaging, over several decades [101]. In the same study it was shown that the frequency spectrum of the particle density, as sampled by a Langmuir probe, varies little with varying inflow rates of the contrast gas, and also varies little when the time series was sampled with and without the contrast gas present. These observations suggest qualitatively that the neutral gas particles have a only a feeble impact on the plasma turbulence.

Figs. 18 presents a series of subsequent images obtained from the gas-puff imaging diagnostics installed in the Alcator C-Mod. It shows the radial motion of a blob structure as viewed in the radial-poloidal domain, with the coordinates given in pixel values. The amplitude of the blob is approximately 3 in units of the fluctuations, normalized to their root-mean square, and has a diameter of approximately 5 mm. The intensity time series measured by the pixel marked with a black dot is presented in Fig. 18. During the blob traversal, the time series shows a fast rise and a slow decay of the intensity, similar to

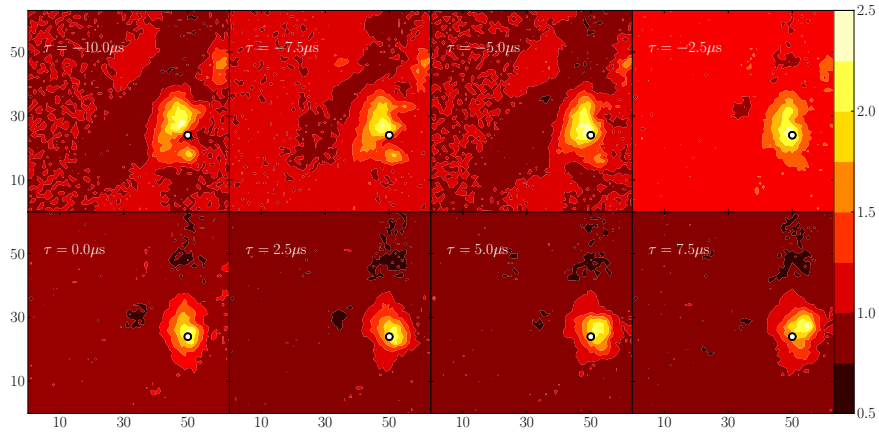


FIG. 17. Blob motion as observed by gas-puff imaging in the scrape-off layer of Alcator C-Mod. The camera views the plasma in the radial (horizontal) - poloidal (vertical) plane.

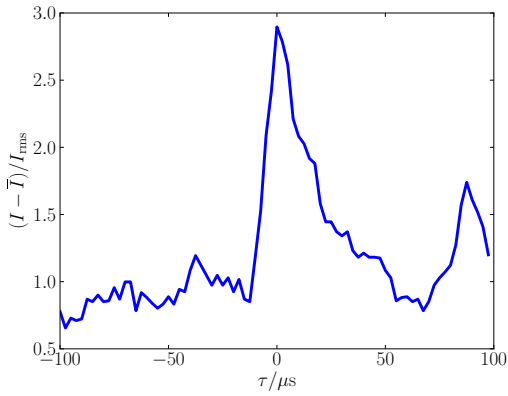


FIG. 18. Intensity time series, as measured by the pixel denoted by the black circle in Fig. 17.

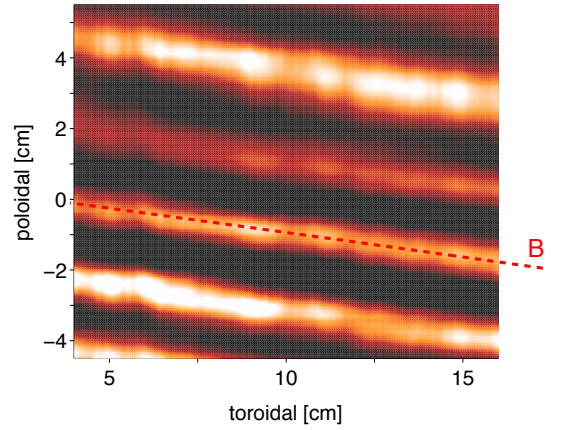


FIG. 19. A blob observed by gas-puff imaging in the scrape-off layer of Alcator C-Mod. The diagnostic views the plasma in the radial-poloidal plane. Source: [64]

the waveform of ion saturation current, Fig. 15. Fig. 19 presents a camera frame, where the plasma is viewed in the toroidal-poloidal plane. It shows plasma filaments which are elongated along the magnetic field.

Paper 3 of this thesis presents an analysis of plasma blob dynamics for data recorded by the gas-puff imaging diagnostic, viewing the outboard mid-plane scrape-off layer of Alcator

C-Mod. For this, a blob tracking algorithm has been developed that tracks the radial and poloidal motion of the plasma blobs in frames captured by a fast CCD camera. This resulted in an original data set consisting of blob sizes and velocities over a broad range of ohmically heated L-mode plasmas with varying line-averaged particle density.

#### 4. *Blob Generation Mechanism and Rate*

The generation of large-amplitude plasma filaments has been studied by numerical simulations in two-dimensional geometry, where the simulation domain models the transition from closed to open field lines [48, 102–105], as well as experimentally in tokamak plasmas [95 and 106], simple toroidal plasma experiments [85, 107–109], and the torsatron TJ-K [110 and 111]. On the other hand, little theoretical work has been done on the generation of large amplitude plasma filaments. In this context the filaments are often denoted as mesoscale structures, since their cross-field size is in between the scale length of the plasma pressure gradient  $L_p$  and the sound gyro radius  $\rho_s$ . So far, no universal generation mechanism for mesoscale structures is unambiguously identified [52, 112, and 113].

Numerical simulations of interchange turbulence of a plasma divided into one region with closed field lines and one region with open field lines showed the intermittent generation of large amplitude plasma filaments at the transition layer [48 and 50]. These filaments would subsequently detach from the transition layer as to propagate radially outwards, developing a steep front and a trailing wake, while mediating large particle flux events. Although not linking this breakup explicitly to a physical mechanism, [48] reveals a correlation between bursts of energy transfer from the a shear flow, as well as from thermal energy to the fluctuating kinetic energy and large-amplitude bursts of the fluctuating energy of the system. The observed statistics in the open field line region were found to be in qualitative agreement with experimental results. Work done in [114] uses a different model, including adiabatic coupling of the electrons to the electric potential in the closed field line region, and related the tear of radial streamers caused by velocity shear layer at the transition region from open to closed field lines to the detachment of plasma blobs. Qualitatively similar results are presented in [104]. This work employed a two-region model, with one simulation plane at the outboard mid-plane and one plane in the X-point region. These two regions are electrically connected and feature flux tube fanning and magnetic shear, while resistivity and

shear are free model parameters. Results of turbulence simulations in this model indicate that for high and low shear, as well as for high and low resistivity, blobs are created at the radial position where the logarithmic derivative of the density profile is maximum. It was further found that this position coincides with the position where the skewness of the particle density fluctuation vanishes. Moreover, it was found that the packing fraction, defined as the average blob duration at a fixed point divided by the average blob waiting time, varies little when changing the geometry or the resistivity [104].

At the simple toroidal plasma device TORPEX, another blob generation mechanism was observed. In this experiment all magnetic field lines intersect material walls. It was observed, that an interchange wave, propagating in the vertical direction at the center of the plasma column, develops radially elongated crests. These crests were found to break off due to a competition between radial and vertical transport [85, 107–109], as to flatten out the gradient of the perturbed plasma pressure that is introduced by the interchange wave.

Experimental studies in tokamak plasmas using gas puff imaging regularly place the blob birth zone close to the separatrix [95, 103, and 106]. As the line-averaged density approaches the Greenwald density, it was further observed that the blob birth region moves inside the separatrix [95] as the pressure gradients begin to smoothly extend from the scrape-off layer into the edge region. This phenomena has been interpreted as to connect the blob birth mechanism to the plasma pressure gradient. Measurements performed at the NSTX tokamak furthermore show a decrease in the total number of blob events as the shear flow velocity at the last closed flux surface increases [106].

The rate by which plasma blobs are generated has been only studied little in the literature. Order of magnitude estimates, based on the fraction of particles that are transported across the separatrix and the geometrical size of the blob, find that the frequency of plasma oscillations that produce blobs is approximately  $\omega \sim 10^4 \text{ s}^{-1}$  [52]. Analysis of the long ion saturation current time series presented in Section VII reveal that the average waiting time between intermittent large-amplitude burst events is approximately  $200 \mu\text{s}$  and changes only little with the plasma parameters. The observation that the waiting time between burst events is exponentially distributed is compatible with the assumption that the arrival times of the individual burst events is uniformly distributed [115].

## II. REDUCED FLUID MODELS FOR MAGNETIZED PLASMAS

In this section, we derive the reduced fluid models that are used in Sections III and IV to study the dynamics of plasma blobs. The aim of these studies was to elucidate the effect of sheath dissipation and dynamical friction on blob dynamics governed by electrostatic advection.

### A. Fluid Modeling

Let us consider a simple plasma, consisting of two particle species, electrons and singly charged ions. We denote the species with an index  $\alpha$ , where  $\alpha = e$  denotes electrons and  $\alpha = i$  denotes ions. The quantity that contains all information about each particle species constituting the plasma is the phase space distribution function  $f_\alpha(\mathbf{x}, \mathbf{v}, t)$ , which assigns the particle density to each point in the phase space  $\mathbf{x} \oplus \mathbf{v}$  at a given time  $t$ . In other words,  $f_\alpha(\mathbf{x}, \mathbf{v}, t)$  is the phase space density of particles of species  $\alpha$  at the position  $\mathbf{x}$  and time  $t$ , having the velocity  $\mathbf{v}$ . The total number of particles of species  $\alpha$  within a phase space volume  $d\mathbf{x} d\mathbf{v}$  is then given by  $f_\alpha(\mathbf{x}, \mathbf{v}, t)d\mathbf{x} d\mathbf{v}$ . The evolution of the phase space density is governed by the Boltzmann equation:

$$\frac{\partial f_\alpha}{\partial t} + \mathbf{v} \cdot \nabla f_\alpha + \frac{\mathbf{F}_\alpha}{m_\alpha} \cdot \nabla_{\mathbf{v}} f_\alpha = \mathcal{C}_\alpha. \quad (11)$$

In this equation, the velocity space del-operator in Cartesian coordinates is given by  $\nabla_{\mathbf{v}} = (\partial/\partial v_x, \partial/\partial v_y, \partial/\partial v_z)$ , and the force acting on a particle of species  $\alpha$  at the point  $\mathbf{x}$  with velocity  $\mathbf{v}$  is the Lorentz force,  $\mathbf{F}_\alpha = \mathbf{F}_\alpha(\mathbf{x}, \mathbf{v}, t) = e_\alpha \mathbf{E}(\mathbf{x}, t) + e_\alpha \mathbf{v} \times \mathbf{B}(\mathbf{x}, t)$ . Here, the electric charge of species  $\alpha$  is given by  $e_\alpha$ . The term on the right hand side,  $\mathcal{C}_\alpha$ , is referred to as the collision term and describes the effect of particle collisions in phase space. Thus, the Boltzmann equation relates the rate of change of the phase space density to the dynamics of the plasma, expressed by its inertia, the Lorentz force, and collisions. Ignoring the effect of collisions, Eqn. (11) reduces to the conservation of phase space density,  $df/dt = 0$ , which is known as the Vlasov equation.

To avoid the detailed kinetic description of the plasma, one often describes the state of the plasma by moments of the distribution function of the particle species

$$\mathcal{M}_{k,\alpha}(\mathbf{x}, t) = \int d^3\mathbf{v} \underbrace{\mathbf{v} \cdots \mathbf{v}}_{k \text{ times}} f_\alpha(\mathbf{x}, \mathbf{v}, t), \quad (12)$$

where  $k = 0, 1, \dots$  denotes the order of the moment and the  $k$ -th moment is a tensor with a maximal rank  $k$  [116]. The infinite set of all moments defines any  $f_\alpha$  uniquely. The  $\mathcal{M}_{k,\alpha}$  also relate to experimentally observable quantities. For example, the zeroth order moment is just the particle density,  $n_\alpha(\mathbf{x}, t) = \int d^3\mathbf{v} f_\alpha$ , the first moment is the particle flux  $\mathbf{\Gamma}_\alpha = n_\alpha(\mathbf{x}, t)\mathbf{u}_\alpha(\mathbf{x}, t) = \int d^3\mathbf{v} \mathbf{v} f_\alpha$ . Here  $\mathbf{u}(\mathbf{x}, t)$  is the mean flow velocity of the plasma. The scalar pressure  $p_\alpha$  may be expressed by the second order moment.

In the same manner, an evolution equation for the  $k$ -th moment is found by multiplying Eqn. (11) with  $\mathbf{v} \cdots \mathbf{v}$  ( $k$ -times) and integrating over velocity space, as outlined in [116]. This procedure results in a conservation law for  $\mathcal{M}_{k,\alpha}$ . A set of evolution equations for the moments  $\mathcal{M}_{k,\alpha}$  are referred to as fluid equations. A problem intrinsic to this procedure is that the evolution equation of the  $k$ -th moment is coupled to the  $(k + 1)$ th moment. For example, the density evolution equation depends on the fluid velocity, and the velocity evolution equation depends on the pressure. Closure of the fluid equations is commonly approached by two different methods, or closure schemes. Asymptotic schemes exploit the smallness of a parameter to truncate the fluid equations. Chapman and Enskog performed this method in the case of a neutral gas, dominated by collisions [117], where it was assumed that the mean-free path of the gas particles is small when compared to the system length. For a fully ionized plasma, a closure of the fluid equation was presented by Braginskii in his much celebrated review article [118]. Less strict truncation schemes allow a quick insight into the dynamics that are described by the fluid equations with the drawback that they include uncontrolled approximations [119]. The *local thermodynamic equilibrium* truncation scheme assumes that the particle distribution function of any plasma particle species is given by a local Maxwellian distribution:

$$f_\alpha(\mathbf{x}, \mathbf{v}, t) = \frac{n_\alpha(\mathbf{x}, t)}{(2\pi)^{3/2} v_{\text{th},\alpha}(\mathbf{x}, t)^2} \exp\left(-\frac{[\mathbf{v} - \mathbf{u}_\alpha(\mathbf{x}, t)]^2}{2v_{\text{th},\alpha}(\mathbf{x}, t)^2}\right). \quad (13)$$

The resulting fluid equations have no associated heat flux, or viscosity, and are given by

$$\frac{\partial n_\alpha}{\partial t} + \nabla \cdot (n_\alpha \mathbf{u}_\alpha) = 0, \quad (14a)$$

$$m_\alpha n_\alpha \left( \frac{\partial}{\partial t} + \mathbf{u}_\alpha \cdot \nabla \right) \mathbf{u}_\alpha = -\nabla p_\alpha + q_\alpha n_\alpha (\mathbf{E} + \mathbf{u}_\alpha \times \mathbf{B}), \quad (14b)$$

$$\left( \frac{\partial}{\partial t} + \mathbf{u}_\alpha \cdot \nabla \right) p_\alpha + \frac{5}{2} p_\alpha \nabla \cdot \mathbf{u}_\alpha = 0. \quad (14c)$$

where we have neglected electron-ion collisions for simplicity. Commonly, the LTE approximation is considered for plasmas that are collisional. Their mean-free path between particle

collisions is small compared to the system length  $L$ ,  $v_{\text{th},\alpha}/\nu_\alpha \ll L$ . In this situation, the distribution function of the particle species has relaxed to a Maxwellian distribution function after a few collision times.

Typical scrape-off layer plasma parameters are  $n_e = 5 \times 10^{19} \text{m}^{-3}$ ,  $T_i \approx T_e = 20 \text{eV}$ , and  $L_\parallel = 10 \text{m}$ . The magnetization parameter and collisionality in this case satisfy

$$\frac{\rho_\alpha}{L_\perp} \ll 1 \quad \frac{\nu_\alpha}{\Omega_{c,\alpha}} \ll 1 \quad \frac{\lambda_{\text{mfp}}}{L_\parallel} \ll 1. \quad (15)$$

This describes the situation, where particles perform several gyrations, with a gyro-radius small to the perpendicular scale of the system, before being subject to a Coulomb collisions. Evaluating these parameters for deuterium ions, we find  $\rho_i/L_\perp \approx 3.2 \times 10^{-2}$ ,  $\nu_i/\Omega_{ci} \approx 0.1$ , and  $\lambda_{\text{mfp}}/L_\parallel \approx 1.6 \times 10^{-4}$ . Corresponding ratios evaluated for the electrons are of similar value. We thus assume a magnetized and collisional scrape-off layer plasma in the following.

## B. Reduced Fluid Model for Blob Simulations

In Cartesian coordinates, with  $x$  in the radial direction,  $y$  along the approximate poloidal direction, and  $z$  along the direction of the magnetic field, the radial plasma flux due to electrostatic advection is given by

$$\Gamma_x = -n \frac{\partial \phi}{\partial y}, \quad (16)$$

where  $\phi$  the electrostatic potential. In this sense, a minimal reduced fluid model needs to include a self consistent evolution of the particle density and the electrostatic potential.

To investigate the effect of sheath dissipation and dynamic friction on electrostatic blob motions, we now continue to derive a reduced fluid model for a quasi-neutral simple plasma that incorporates a constant electron temperature, cold ions, as well as vanishing electron inertia:

$$\frac{T_e}{T_i} \ll 1, \quad \frac{m_e}{m_i} \ll 1, \quad \frac{|n_e - n_i|}{n_e} \ll 1. \quad (17)$$

Motivated by the observation that the correlation length of fluctuations in scrape-off layer plasmas is large compared to their correlation length perpendicular to the magnetic field, we order the wave numbers of the fluctuations as

$$k_\perp \gg k_\parallel. \quad (18)$$

This ordering is commonly referred to as flute ordering. The anisotropy of the fluctuation wave numbers is used to simplify the advective derivative in the fluid equations. Separating the fluid velocity field into components parallel and perpendicular to the magnetic field as  $\mathbf{V} = \mathbf{V}_\perp + \mathbf{V}_\parallel$ , an order of magnitude estimate of the advective derivative shows that

$$\mathbf{V} \cdot \nabla = \mathbf{V}_\perp \cdot \nabla_\perp + \mathbf{V}_\parallel \cdot \nabla_\parallel \approx \mathbf{V}_\perp \cdot \nabla_\perp + \mathcal{O}\left(\frac{k_\parallel}{k_\perp}\right),$$

provided that  $V_\perp \approx V_\parallel$ . The unit vector along the magnetic field is given by  $\mathbf{b} = \mathbf{B}/|\mathbf{B}|$ , where  $|\cdot|$  denotes the vector norm.

With flute ordering at hand, we now introduce the drift approximation. This denotes the reduction of a differential equation for the fluid cross field velocity to an algebraic equation, by applying the so-called drift operator,  $\mathbf{b} \times$ , to the momentum equation. As a result, the constituents of the fluid cross-field drifts become evident. In the approximations given by Eqn. (17), the fluid equations for the electrons and ions, in contact with a neutral gas at rest, are given by

$$m_i n \left( \frac{\partial}{\partial t} + \mathbf{u}_i \cdot \nabla \right) \mathbf{u}_i = en(\mathbf{E} + \mathbf{u}_i \times \mathbf{B}) - m_i n \nu_n \mathbf{u}_i, \quad (19a)$$

$$0 = -\nabla p_e - en(\mathbf{E} + \mathbf{u}_e \times \mathbf{B}). \quad (19b)$$

Here, the frequency of elastic collisions between the ions and the gas atoms is given by  $\nu_n$ . We obtain the cross field drift of the electrons and ions by applying the drift operator  $\mathbf{b} \times$  to their respective momentum equations and successively solve for the perpendicular component of the velocity. This gives

$$\begin{aligned} \mathbf{u}_{e,\perp} &= \frac{\mathbf{E} \times \mathbf{B}}{B^2} - \frac{1}{neB} \mathbf{b} \times \nabla p_e, \\ \mathbf{u}_{i,\perp} &= \frac{\mathbf{E} \times \mathbf{B}}{B^2} + \frac{1}{\Omega_{ci}} \mathbf{b} \times \frac{d\mathbf{u}_{i,\perp}}{dt} - \frac{\nu_n}{\Omega_{ci}} \mathbf{b} \times \mathbf{u}_i. \end{aligned}$$

These components are readily identified as the electric drift, the electron diamagnetic drift, the ion polarization drift, and the resistive drift:

$$\begin{aligned} \mathbf{u}_E &= \frac{\mathbf{E} \times \mathbf{B}}{B^2}, & \mathbf{u}_d &= -\frac{1}{enB} \mathbf{b} \times \nabla p_e, \\ \mathbf{u}_{\text{pol}} &= \frac{1}{\Omega_{ci}} \mathbf{b} \times \frac{d\mathbf{u}_{i,\perp}}{dt}, & \mathbf{u}_r &= \frac{\nu_n}{\Omega_{ci}} \mathbf{b} \times \mathbf{u}_{i,\perp}. \end{aligned}$$

The cross-field drift of the electrons is comprised by the electric drift and the diamagnetic drift. Their polarization drift vanishes as we have neglected electron inertia. The cross-field

drift of the ions is comprised by the electric drift, the polarization drift, and the resistive drift. The diamagnetic ion drift vanishes as we consider cold ions. Both the electron diamagnetic drift and the ion polarization drift are charge dependent. However, the magnitude of the ion polarization drift is smaller than the magnitude of the electric drift by a factor of  $\Omega/\Omega_{ci}^{-1}$ , where  $\Omega$  is the characteristic magnitude of the frequency, i. e.  $\Omega \sim \partial/\partial t$ . It is this drift that contributes predominantly to the electric polarization of the plasma.

We continue the derivation by computing the divergences of the particle drifts. These will subsequently be used in Eqn. (5) as to obtain evolution equations for the particle density and the plasma vorticity. For the compression of the electric drift and the electron diamagnetic drift we find

$$\begin{aligned}\nabla \cdot \mathbf{u}_E &= \frac{1}{B} (\mathbf{b} \times \nabla \ln B + \nabla \times \mathbf{b}) \cdot \nabla \phi, \\ \nabla \cdot (n\mathbf{u}_d) &= -\frac{1}{eB} (\mathbf{b} \times \nabla \ln B + \nabla \times \mathbf{b}) \cdot \nabla p_e.\end{aligned}$$

Their similar structure motivates the definition of the curvature operator  $\mathcal{K}(\cdot)$  which is defined by its action on a scalar field  $u$  as

$$\mathcal{K}(u) = \frac{1}{B} (\mathbf{b} \times \nabla \ln B + \nabla \times \mathbf{b}) \cdot \nabla u. \quad (20)$$

Both inhomogeneity of the magnetic field, given by  $\nabla_{\perp} \ln B$ , and its curvature, given by  $\nabla \times \mathbf{b}$ , cause a compression of the respective drifts. In slab geometry, where the  $x$  coordinate is along the major radius, the  $y$  coordinate is approximately along the poloidal coordinate at outboard midplane, and the  $z$  coordinate is along the magnetic field, the curvature operator can be simplified. For this, we note that the magnetic curvature is defined as the change of the magnetic field, projected along its unit vector, for which the identity

$$\boldsymbol{\kappa} = \mathbf{b} \cdot \nabla \mathbf{b} = -\mathbf{b} \times (\nabla \times \mathbf{b}) \quad (21)$$

holds [2]. For a purely toroidal magnetic field,  $\mathbf{B} = -(B_0 R_0/R)\mathbf{e}_{\zeta}$ , the inhomogeneity of the magnetic field is given by  $\nabla \ln B \approx -(1/R)\mathbf{e}_x$  and its curvature is given by  $\nabla \times \mathbf{b} \approx -(1/R)\mathbf{e}_y$ , see Section A. This approximation follows from neglecting plasma currents in Ampère's law,  $\nabla \times \mathbf{B} = B\nabla \times \mathbf{b} + \nabla B \times \mathbf{b} = \mathbf{0}$ . The magnetic field is thus given only by external currents to lowest order.

With the curvature operator in the slab approximation given by

$$\mathcal{K}(u) = -\frac{2}{BR} \frac{\partial u}{\partial y}, \quad (22)$$

we evaluate the compression of the electric and the electron diamagnetic drift to be

$$\nabla \cdot \mathbf{u}_E = -\frac{2}{BR} \frac{\partial \phi}{\partial y}, \quad (23)$$

$$\nabla \cdot (-en\mathbf{u}_d) = \frac{2T_e}{BR} \frac{\partial n_e}{\partial y}. \quad (24)$$

Anticipating that the electric drift dominates the cross field ion dynamics, we evaluate the compression of the ion polarization current iteratively

$$\begin{aligned} \nabla \cdot (en\mathbf{u}_{\text{pol}}) &= \nabla \cdot \left( \frac{m_i n}{B} \mathbf{b} \times \frac{d\mathbf{u}_E}{dt} \right) \\ &\approx m_i \left( \frac{1}{B^2} \nabla n \cdot \frac{d\nabla_{\perp} \phi}{dt} - n \frac{\nabla \ln B}{B} \cdot \frac{d\nabla_{\perp} \phi}{dt} + \frac{n}{B^2} \frac{d\nabla_{\perp}^2 \phi}{dt} \right). \end{aligned}$$

Assuming a homogeneous background plasma, and anticipating that perturbations of the particle density and of the electric potential are due to a plasma blob, we estimate the length scale of the perturbations to be  $\nabla_{\perp} \ln n \sim \nabla_{\perp} \ln \phi \sim \ell^{-1}$ . On the other hand, the magnetic field varies on a length scale given by the major radius,  $\nabla_{\perp} \ln B \sim 1/R_0$ . We therefore neglect the middle term and commute  $\nabla \cdot$  with  $d/dt$ . In the context of reduced fluid modeling, the Boussinesque approximation is often used [69, 73, 79, 104, 120, and 121], by whose virtue we neglect the first term on the right hand side in the last equation.<sup>122</sup> In this approximation, the compression of the ion polarization current reads

$$\nabla \cdot (en\mathbf{u}_{\text{pol}}) = \frac{en}{\Omega_{ci} B} \frac{d\nabla_{\perp}^2 \phi}{dt}. \quad (25)$$

Finally, the compression of the resistive current is given by

$$\nabla \cdot (en\mathbf{u}_r) = -\frac{\nu_n}{\Omega_{ci}} en \frac{\nabla_{\perp}^2 \phi}{B}. \quad (26)$$

With expressions for the compression of the currents at hand, we continue to derive a reduced two-fluid model. For this, we introduce the plasma vorticity

$$\mathbf{b} \cdot \nabla \times \mathbf{u}_E = \frac{1}{B} \mathbf{b} \cdot \left[ -\frac{\nabla B}{B} \times (\mathbf{b} \times \nabla \phi) + (\nabla \phi \cdot \nabla \mathbf{b} - \nabla \phi \nabla \cdot \mathbf{b}) + (\mathbf{b} \nabla^2 \phi - \mathbf{b} \cdot \nabla \nabla \phi) \right].$$

The right hand side can be grouped in terms, where  $\nabla$  acts only on  $\phi$ , the terms in the rightmost bracket, and terms where  $\nabla$  acts on both,  $\mathbf{b}$ , and  $\phi$ . With the approximation  $L_{\perp} \ll R$ , the electric drift vorticity reduces to

$$\mathbf{b} \cdot \nabla \times \mathbf{u}_E \approx \frac{1}{B} \nabla_{\perp}^2 \phi \equiv \Omega, \quad (27)$$

so that we may express the electrostatic dynamics by a scalar variable, the electric drift vorticity.

Having the compression of all drifts at hand, we continue by evaluating Eqn. (5b), using Eqs. (23) - (25), and (26):

$$\nabla \cdot \mathbf{J}_\perp = \nabla (en\mathbf{u}_{\text{pol}} + en\mathbf{u}_r - en\mathbf{u}_d) = -\nabla \cdot \mathbf{J}_\parallel.$$

The advective derivative is often formulated using Poisson brackets  $\{\phi, f\}$ , defined via

$$\mathbf{u}_E \cdot \nabla f = \frac{1}{B} \left( \frac{\partial \phi}{\partial x} \frac{\partial f}{\partial y} - \frac{\partial \phi}{\partial y} \frac{\partial f}{\partial x} \right) \equiv \frac{1}{B} \{\phi, f\}. \quad (28)$$

Inserting the expressions for the compression of the electron diamagnetic drift, Eqn. (24), and the compression of the ion polarization drift, Eqn. (25), yields the vorticity equation

$$\frac{\partial \Omega}{\partial t} + \frac{1}{B} \{\phi, \Omega\} + \frac{2C_s^2}{R} \frac{\partial \ln n}{\partial y} + \frac{\nu_n}{\Omega_{\text{ci}}} \Omega = -\frac{\Omega_{\text{ci}}}{en} \nabla_\parallel \cdot \mathbf{J}_\parallel. \quad (29)$$

We further use the electron continuity equation as an evolution equation for the particle density. With Eqs. (23) and (24), this gives

$$\frac{\partial \ln n}{\partial t} + \frac{1}{B} \{\phi, \ln n\} - \frac{2n}{BR} \frac{\partial \phi}{\partial y} - \frac{2C_s^2}{\Omega_{\text{ci}} R} \frac{\partial \ln n}{\partial y} = 0. \quad (30)$$

Together with Eqn. (29), this is the reduced fluid model.

To obtain a set of normalized equations, suitable for numerical simulations, we normalize spatial and temporal scales, as well as the electrostatic potential via

$$\nabla \rightarrow \nabla' = \ell \nabla \quad \frac{\partial}{\partial t} \rightarrow \frac{\partial}{\partial t'} = \frac{1}{\gamma} \frac{\partial}{\partial t} \quad \phi \rightarrow \phi' = \frac{\phi}{\gamma B \ell^2}. \quad (31a)$$

Here we define the ideal interchange rate

$$\gamma = \sqrt{\frac{g}{\ell}}, \quad (32)$$

where  $g = 2C_s^2/R$  is the effective gravity. The normalization of the electrostatic potential by the characteristic length-, and time-scale is chosen as to minimize the number of model parameters. Anticipating that the electric current is determined by the sheath boundary condition Eqn. (4), we furthermore normalize the current as  $\mathbf{J} \rightarrow \mathbf{J}' = \mathbf{J}_\parallel / enC_s$ , giving a term of order unity.

The resulting normalized equations are given by

$$\frac{\partial \ln n}{\partial t} + \{\phi, \ln n\} - 2 \frac{\ell}{R} \frac{\partial \phi}{\partial y} - \frac{\gamma}{\Omega_{\text{ci}}} \frac{\partial \ln n}{\partial y} = 0 \quad (33a)$$

$$\frac{\partial \Omega}{\partial t} + \{\phi, \Omega\} + \frac{2C_s^2}{\gamma^2 R \ell} \frac{\partial \ln n}{\partial y} + \frac{\nu_n}{\gamma} \Omega = -\frac{\Omega_{\text{ci}} C_s}{L_\parallel \gamma^2} \nabla_\parallel \cdot \mathbf{J}_\parallel \quad (33b)$$

where here and in the following we have suppressed the prime. Explicitly, we normalize temporal scales to the ideal interchange rate where  $g = 2C_s^2/R$  is the effective gravity. Although the compression of the diamagnetic flux is of the order  $\rho_s/\sqrt{R\ell}$ , we neglect this term as previous numerical studies revealed that it only contributes marginally to the cross-field dynamics [123], while on the other hand introducing another parameter into the model. We also neglect the compression of the electric drift since  $\ell \ll R$ .

In the spirit of flute ordering, we now assume long wavelengths along the magnetic field and define a field line-average operator by

$$\langle f(x, y, s) \rangle = \frac{1}{L_{\parallel}} \int_{-L_{\parallel}/2}^{L_{\parallel}/2} ds f(x, y, s) = f_0(x, y). \quad (34)$$

Here,  $s$  is the coordinate along the magnetic field. Then, any smooth scalar field may be decomposed into its mean value along the magnetic field,  $\langle f \rangle$ , and a local perturbation  $\tilde{f}(x, y, s)$ . The field line average of a perturbation vanishes by virtue of Eqn. (34). Applying Eqn. (34) to Eqs. (33), yields

$$\frac{\partial \ln \langle n \rangle}{\partial t} + \{ \langle \phi \rangle, \ln \langle n \rangle \} = 0, \quad (35a)$$

$$\frac{\partial \langle \Omega \rangle}{\partial t} + \{ \langle \phi \rangle, \langle \Omega \rangle \} + \frac{\partial \ln \langle n \rangle}{\partial y} + \nu \langle \Omega \rangle = \frac{\Omega_{ci} C_s}{\gamma^2 B} \langle \nabla_{\parallel} \cdot \mathbf{J}_{\parallel} \rangle. \quad (35b)$$

where  $\nu = \nu_n/\gamma$ . These equations describe the plasma dynamics perpendicular to the magnetic field where the parallel dynamics are parameterized by the field-line average of the compression of the parallel currents. In this sense, Eqs. (33) is the simplest possible model for a self-consistent description of the radial particle flux, Eqn. (16), on a two-dimensional plane perpendicular to the magnetic field.

### 1. Sheath Dissipation

In Section III of this thesis we employ Eqs. (35) to study the effects of sheath dissipation on the radial propagation of blobs and neglect friction by setting  $\nu = 0$ . This describes damping of the plasma motions due to electric currents entering the sheaths which form where magnetic field lines intersect material walls. Evaluating  $\langle \nabla_{\parallel} \cdot \mathbf{J}_{\parallel} \rangle$  with the sheath boundary condition, Eqn. (4), we find the coefficient which parameterizes the parallel dy-

namics to be

$$\Lambda = \frac{C_s \ell^2}{\rho_s^2 \gamma L_{\parallel}} = \left( \frac{\ell}{\ell_*} \right)^{5/2} \quad (36)$$

in dimensionless units, or  $\sigma = C_s/\rho_s^2 L_{\parallel}$  in dimensional units. The vorticity equations now reads

$$\frac{\partial \langle \Omega \rangle}{\partial t} + \{ \langle \phi \rangle, \langle \Omega \rangle \} + \frac{\partial \ln \langle n \rangle}{\partial y} + \nu \langle \Omega \rangle = -\Lambda \langle \phi \rangle$$

The size  $\ell_*$  is defined as the length scale on which the magnitude of all terms in Eqn. (33b) balance when  $\nu = 0$  [69]. For  $\Lambda \ll 1$ , electric currents induced by magnetic curvature and magnetic inhomogeneity are closed by polarization currents. For  $\Lambda \gg 1$  they are closed by electric currents to the sheaths. As discussed in Section III,  $\Lambda$  represents a geometrical quantity as  $\Lambda = \ell^{5/2} R^{1/2} / \rho_s^2 L_{\parallel}$ . A variation of this parameter may be interpreted as a variation in ratio of the blob length to the ion thermal gyro radius, while holding the connection length and the major radius constant.

The main effect of sheath dissipation on the perpendicular dynamics is a damping of the collective motions on large spatial scales. To see this, we note that  $\Omega = \nabla_{\perp}^2 \phi$  and assume plane wave perturbations on a homogeneous plasma equilibrium of the form  $\exp(i[k_x x + k_y y - \omega t])$ , where  $k_x$  and  $k_y$  are the wave numbers in the plane normal to the magnetic field and  $\omega$  is the frequency of the perturbation. Considering only the inertial term and the sheath dissipation term in Eqn. (35b), we find the dispersion relation to be

$$\omega = -i \frac{\Lambda}{k_{\perp}^2}, \quad (37)$$

with  $k_{\perp}^2 = k_x^2 + k_y^2$ . This is just exponential damping acting predominantly on large spatial scales.

One limitation of the approach to parameterize the parallel dynamics of the system is that the field-line average of perturbation vanishes only for linear terms. The field-line average of a non-linear term is generally non-vanishing:

$$\langle f(x, y, s) \cdot g(x, y, s) \rangle = \langle f \rangle(x, y) \langle g \rangle(x, y) + \langle \tilde{f}(x, y, s) \cdot \tilde{g}(x, y, s) \rangle. \quad (38)$$

Thus, the field-line averaged equations, Eqn. (35), are only valid in the limit where none of the fields have any variation along the magnetic field.

## 2. Dynamical friction

In the limit of strong plasma resistivity, the parallel dynamics in the model may be neglected by setting  $\langle \nabla_{\parallel} \cdot \mathbf{J}_{\parallel} \rangle = 0$ . In this case, the field-line averaged equations, Eqs. (35) and (33), are mathematically identical. The latter models the situation where the balance between polarization currents, diamagnetic currents, and resistive currents in the drift plane are governed by the normalized friction parameter

$$\nu = \sqrt{\frac{\ell}{g}} \nu_n. \quad (39)$$

As discussed in Section IV, this implies that the ratio between the blob size  $\ell$  and the frictional length scale  $g/\nu_n^2$  determines this balance.

Collisional friction acts as a monochromatic damping on the collective cross field dynamics, as described by the plasma vorticity. As in the discussion of sheath dissipation, we assume plane wave perturbations for the vorticity to find the dispersion relation of Eqs. (33b) in the absence of the interchange term

$$\omega = -i\nu. \quad (40)$$

This results in qualitatively different dynamics for the cases where sheath dissipation and dynamical friction are the acting dissipation mechanisms and also in qualitative differences of the transition from inertial velocity scaling regime to, respectively, the sheath dissipative and frictional velocity scaling regime.

We have assumed neither drift ordering or MHD ordering. When considering drift ordering, we should include  $\nabla \cdot (n\mathbf{u}_d)$  in the continuity equation, Eqn. (33a), because this is the only term where  $\rho_s$  enters explicitly. In this sense, dynamics described by the model Eqs. (33) is inherent to both, MHD models and fluid models in drift ordering.



**III. PAPER 1: VELOCITY SCALING FOR FILAMENT MOTION IN SCRAPE-OFF LAYER PLASMAS**

Published in Physics of Plasmas **18**, 102314 (2011)

Authors: R. Kube and O. E. Garcia

**IV. PAPER 2: INTERCHANGE MOTION OF LARGE AMPLITUDE PLASMA  
FILAMENTS**

Published in Physics of Plasmas **19**, 042305 (2012)

Authors: R. Kube and O. E. Garcia

**V. PAPER 3: BLOB SIZES AND VELOCITIES IN THE ALCATOR C-MOD  
SCRAPE-OFF LAYER**

Journal of Nuclear Materials **438** S505-S508 (2013)

Authors: R. Kube, O. E. Garcia, B. LaBombard, J. L. Terry and S. J. Zweben

**VI. PAPER 4: CONVERGENCE OF STATISTICAL MOMENTS OF PARTICLE DENSITY TIME SERIES IN SCRAPE-OFF LAYER PLASMAS**

Submitted to Physics of plasmas.

Available online at <http://arxiv.org/abs/1409.8319>

Authors: R. Kube and O. E. Garcia

**VII. PAPER 5: FLUCTUATION STATISTICS IN THE SCRAPE-OFF LAYER OF  
ALCATOR C-MOD**

To be submitted.

Available online at <http://arxiv.org/abs/1410.4114>

Authors: R. Kube, O. E. Garcia, B. LaBombard, and J. Terry

## VIII. SUMMARY, CONCLUSIONS AND OUTLOOK

### A. Summary and Conclusions

The work presented in this thesis can be divided into two parts. Part one studies the dynamics of plasma blobs by numerical simulations as well as by analysis of optical measurements of scrape-off layer plasmas. Part two studies the statistical properties of fluctuations in scrape-off layer plasmas.

Numerical simulations of a reduced, two-dimensional fluid model reveal the dynamics of electrostatic blob motion when subject to damping by either sheath dissipation, or dynamical friction. Sheath dissipation arises due to electric currents to the sheath, where the magnetic field lines intersect material walls. This is believed to be a relevant damping mechanism on blob propagation in low resistivity plasmas. For  $\Lambda = 0$ , a blob accelerates radially outwards and develops a mushroom shaped form. Its associated electrostatic potential is dipolar and large compared to the blobs cross-field size. After an initial acceleration, small scale flows break up the coherent blob structure, which leads to a deceleration of the blob. The maximal radial blob velocity depends on the initial amplitude of the blob, relative to the background density, as  $v_{\text{rad}} \sim \sqrt{\Delta n/N}$ . Numerical simulations with  $\Lambda > 0$  reveal that sheath dissipation impedes radial blob propagation. Blobs do not develop a mushroom shape and the scale length of the electric potential is comparable to the blobs cross-field size. With increasing magnitude of  $\Lambda$ , the blobs acceleration phase shortens. This results in a decreasing maximal radial blob velocity as  $\Lambda$  increases. Increasing the initial relative blob amplitude counteracts the damping due to sheath dissipation. For a given value of  $\Lambda$ , a blob with larger initial relative amplitude,  $\Delta n/N$ , accelerates over a longer period of time as to attain a larger maximal radial velocity. For small  $\Delta n/N$ , we find  $v_{\text{rad}} \sim (\Delta n/N)^\alpha$ , where  $\alpha$  is approximately 0.5. For large  $\Delta n/N$  this scaling breaks and the maximal radial blob velocity is independent of the blobs initial relative amplitude. To parameterize the effect of sheath dissipation on the blob velocity by the blobs cross-field size  $\ell$ , the maximal radial blob velocities from the numerical simulations are fitted to an order of magnitude estimate of the plasma vorticity equations. The resulting fit coefficients are used to parameterize the maximum radial blob velocity in terms of the initial blob amplitude and its cross-field size. This reveals that with increasing blob cross-field size  $\ell$ , the blob velocity increases as

$v_{\text{rad}} \sim \sqrt{\ell}$  for small blobs, while  $v_{\text{rad}} \sim \ell^{-2}$  holds for blobs with large cross-field size. Blobs of an intermediate cross-field size propagate with a maximum velocity. The cross-field size for maximal radial velocity is found to vary weakly with the blobs initial amplitude.

The case where damping is due to dynamical friction describes a monochromatic damping of the vorticity. Numerical simulations show that the electric potential of the blob varies on spatial scales that are large compared to the blobs cross-field size. For a given  $\Delta n/N$ , an increasing value of  $\nu$  leads to a more stagnant blob. As in the case of sheath dissipation, the duration over which the blob accelerates, decreases. This leads to a stagnant blob for large values of  $\nu$ . For a given  $\nu$  and a small initial blob amplitude, the maximal radial velocity of the blob depends as a power law on  $\Delta n/N$ . For large blob amplitudes the maximum radial velocity depends only weakly on  $\Delta n/N$ . The dimensional blob velocity is found by fitting the radial velocity, as found by the numerical simulations, on an order of magnitude estimate of the vorticity. Again, the resulting fit coefficients are used to parameterize the maximum radial blob velocity in terms of  $\Delta n/N$  and  $\ell$ . This shows that for a given  $\Delta n/N$ , the blob velocity increases as  $v_{\text{rad}} \sim \sqrt{\ell}$  for small  $\ell$ . For large  $\ell$ , the blob velocity is independent of  $\ell$  and inversely proportional to  $\nu_n$ . The cross-field size, where the velocity scaling transits from the inertial regime into the frictional velocity scaling regime, depends sensitively on the initial blob amplitude.

Damping due to dynamical friction and sheath dissipation has been found to affect blob dynamics in several toroidal plasma devices. At the VTF facility, it was observed that blobs with large amplitude relative to the background may approach a radial velocity comparable to the acoustic velocity [89]. Other features observed in experiments at VTF that agree with the numerical simulations presented in Section IV are the spatio-temporal evolution of the blob, especially its mushroom shape, a dipolar structure of the electric potential which extends over the blobs cross-field size, and the inverse scaling of the velocity with neutral gas pressure. The radial propagation of blobs in a toroidal plasma was also studied at the TORPEX device [140]. Here, the toroidal magnetic field intersects material surfaces and sheath currents affect the blob dynamics. A similar velocity scaling as in Paper 1 was derived. Experiments where  $\ell$  was varied by changing the ion mass are in good agreement with the inertial and sheath-dissipative velocity scaling [140].

As part of this thesis work, a solver for the reduced fluid equations that utilizes the graphical processing unit has been developed. The design goal of this solver was speed and

flexibility, as to employ it for the solving a variety of reduced fluid models.

Analysis of optical measurements of scrape-off layer plasma fluctuations allow a direct measurement of blob dynamics. A blob tracking algorithm for data, obtained by fast camera imaging of gas puff emissions in the scrape-off layer of Alcator C-Mod, has been developed and was used to analyze blob dynamics for several plasma discharges where the line-averaged particle density is varied. We find, that the radial and poloidal length of the plasma blobs depends weakly on the line-averaged particle density. Typical cross field sizes are given by  $\ell \approx 6$  mm, or approximately  $2.5\ell_*$ . While the radial blob velocity increases on average with the line averaged particle density, the poloidal velocity depends only weakly on it and is predominantly in the ion diamagnetic drift direction. We further find that the sheath connected velocity scaling gives a good approximation of the observed radial blob velocities for small line averaged electron densities. For large line-averaged particle densities, it underestimates the observed radial blob velocities.

This comparison between observed radial blob velocities and the prediction of a two-dimensional model should be taken with a grain of salt. Since the underlying model parameterizes the parallel dynamics, an agreement between the observed radial velocities with the sheath connected velocity scaling does not imply that this parameterization accurately describes the physical mechanism determining the radial blob velocity. On the other hand, the deviation between the observed radial velocities and the velocity predicted from the sheath-connected velocity scaling implies that the model is incomplete. As discussed in Section VII however, is the conditionally averaged waveform of the electric potential, as measured at the divertor, compatible with the footprint signature expected when extending the electric potential dipole of a plasma blob along the magnetic field. As further shown in [65], are fluctuations, due to particle density perturbations, sampled at the outboard midplane and at the divertor position along the same magnetic flux tube, highly correlated in the case of low line-averaged particle densities. These three observations together suggest that the electric connection between the outboard midplane and the sheath at the divertor may be relevant a relevant current channel in the electric circuit represented by the blob for plasmas with a low line-averaged particle density.

An alternative approach of studying turbulence is by analyzing the statistic properties of the plasma fluctuations. Recent work models the particle density time series, as measured in scrape-off layer plasmas, as the realization of a stochastic process [94]. This process

assumes that fluctuations, as measured by single-point diagnostics, are due to the radial motions of blob-like structures. The sampled waveform is therefore modeled as a superposition of pulses with a fixed shape and exponentially distributed waiting times and pulse amplitudes. The stationary particle density amplitude distribution function of this model is a Gamma distribution. This distribution is found to describe time series of scrape-off layer fluctuations over several decades in normalized probability [134]. As part of this thesis work, a method to assess mean-squared errors on estimators for the mean, variance, skewness and kurtosis for the realization of such a process was developed. The errors are given as a function of sample length, sampling frequency and the parameters of the stochastic process. We find that the mean squared error on the estimator of the sample mean is proportional to the square of the ensemble average of the underlying stochastic process, inversely proportional to the intermittency parameter  $\gamma$ , and inversely proportional to the number of samples  $N$ . In the limit of a high sampling frequency and large number of samples, the mean squared error also depends on the ratio of the pulse decay time to the sampling frequency.

A bridge between direct numerical simulation of seeded blobs, the spatially resolved measurements by gas-puff imaging, and stochastic modeling of single point measurements is presented in Section VII. Fluctuation statistics of long time series, up to one second, of the particle density and the floating potential, as sampled by Langmuir probes, dwelling in the far scrape-off layer and installed in the lower divertor baffle of the Alcator C-Mod tokamak were analyzed. These time series were obtained in experiments dedicated to study the fluctuations in scrape-off layer plasmas. We confirm that their dynamics are governed by the intermittent arrival of large amplitude burst events. Comparing the probability distribution function of the ion saturation current time series to prevalent analytic models, we find that no model can be discarded. The waiting time between successive large amplitude burst events are well described by an exponential distribution. At the outboard midplane position, Typical scale lengths are given by  $\tau_w \approx 120 \mu\text{s}$  for a low line-averaged density and up to  $200 \mu\text{s}$  for high line-averaged density plasmas. At the divertor, typical scale lengths are given by  $\tau_w \approx 270 \mu\text{s}$  for a low density plasmas and  $\tau_w \approx 380 \mu\text{s}$  for a high density plasma. Employing conditional averaging, the dynamics of the time series are linked to the radial propagation of plasma blobs for the time series obtained in the far scrape-off layer. The conditionally averaged waveforms, as sampled by the divertor probes, present a similar shape. This waveform varies weakly with the line-averaged particle density and presents a

similar shape as the waveform obtained at outboard midplane. The dipolar waveform of the conditionally averaged potential, as sampled at the divertor, is dipolar and similar to the conditionally waveform sampled at outboard mid-plane in the case of small line-averaged particle densities. In the case of large line-averaged particle density, the waveform is not reproducible. This is compatible with an electric disconnection of the plasma blobs from the sheaths formed at the divertor targets.

## B. Outlook

An evident first step is to address the parallel dynamics of seeded plasma blobs. Using a self-consistent three-dimensional model to study the parallel dynamics of a seeded plasma blob allows to address several unresolved issues. As a first step, the parallel expansion of a plasma blob along the magnetic field, including Ohm's law to self-consistently model parallel currents, should be studied. Extending to an electromagnetic model, the effect of outgoing Alfvén waves should also be addressed. This could clarify on what time scale damping of the vorticity dynamics due to outgoing Alfvén waves is important. Furthermore, the effect of magnetic shear should be addressed. Such work should be set in context with previous work where these effects have been parameterized by the WKB limit [79 and 104] to the other kinds of closures. Recent measurements confirmed that the ion temperature is not negligible in the scrape-off layer [154]. Numerical simulations of seeded blobs, which include the effect of warm ions, further show that they may significantly alter the blob dynamics from the cold ion case [155 and 156]. Continuing numerical work to incorporate ion temperature and spatially resolved parallel dynamics should be attempted to give a more complete understanding of plasma transport by blob-like structures in scrape-off layer plasmas.

On the other hand, recent tools to measure particle density, electron temperature, and the plasma potential [157] allow for fluctuation measurements of unprecedented detail in scrape-off layer plasmas. Analysis of this data will allow to address the importance of electron temperature fluctuations as well the of the statistical properties of the radial particle, and heat fluxes.

## ACKNOWLEDGMENTS

Coming to the end of my time as a doctoral student, several acknowledgements need to be made. I would like to thank my supervisor, Odd Erik Garcia, for his superb guidance, motivation and for reading this thesis thoroughly. He generously shared his keen scientific insight with me, and has been a source of great inspiration throughout my time in Tromsø. Next, I would like to thank Drs. Brian LaBombard and Jim Terry for hosting me at MIT. It was inspiring to work with such talented physicist. My stay at PSFC and working with the Alcator C-Mod team made me realize just how big the field of plasma physics and controlled fusion really is. I would like to thank Prof. Kendl for hosting me at the University of Innsbruck and many fruitful discussions on numerics and turbulence. Also thank you Ole and Matthias for an enjoyable time in Innsbruck. Back on the local front, I would like to thank my favorite office mates Daniel and Felix for good discussions and uplifting chatter. And last, but not least thank you Daniela for keeping always keeping me grounded and your support.

## Appendix A: Simple toroidal coordinates

To describe the magnetic field of a toroidally confined plasma one commonly uses flux coordinates  $(\chi, \theta_f, \zeta_f)$ , where  $\chi$  is a generalized radial coordinate which measures the integrated magnetic flux and  $\theta_f$  and  $\zeta_f$  are generalized angular coordinates. In flux coordinates magnetic field lines are straight lines. This is in the sense that the components of the magnetic field along the surface normal vector of the any angular coordinate is a flux quantity:

$$\frac{1}{q(r)} = \frac{\mathbf{B} \cdot \nabla \theta}{\mathbf{B} \cdot \nabla \zeta}. \quad (\text{A1})$$

The quantity  $q(r)$  is called the safety factor and gives the local pitch of the magnetic field lines. It is related to the toroidal transform  $\iota$ , which measures the poloidal displacement following a magnetic field line for one toroidal revolution, via

$$\iota = \frac{\Delta \theta}{\text{one toroidal transit}} = \frac{2\pi}{q(r)}. \quad (\text{A2})$$

Simple toroidal coordinates approximate the magnetic geometry of a toroidally confined plasma while omitting the complicated description in terms of magnetic flux coordinates. Writing Cartesian coordinates as  $\mathbf{x} = (x, y, z)$ , we define simple toroidal coordinates  $(r, \theta, \zeta)$  by the transformation

$$r = \sqrt{y^2 + u^2} \quad \theta = \tan^{-1} \frac{y}{u} \quad \zeta = \tan^{-1} \frac{z}{x}, \quad (\text{A3})$$

where  $u = \sqrt{x^2 + z^2} - R_0$ . The total distance of a point to the symmetry axis is given by  $R = R_0 + r \cos \theta$ . The inverse transformation of the coordinates is accordingly

$$x = (R_0 + r \cos \theta) \cos \zeta \quad y = r \sin \theta \quad z = (R_0 + r \cos \theta) \sin \zeta.$$

In Fig. 53 shows the coordinate system together with a purely toroidal magnetic field. The Jacobian matrix of Eqn. (A3) is given by

$$\mathcal{J} = \begin{pmatrix} \frac{\partial x}{\partial r} & \frac{\partial x}{\partial \theta} & \frac{\partial x}{\partial \zeta} \\ \frac{\partial y}{\partial r} & \frac{\partial y}{\partial \theta} & \frac{\partial y}{\partial \zeta} \\ \frac{\partial z}{\partial r} & \frac{\partial z}{\partial \theta} & \frac{\partial z}{\partial \zeta} \end{pmatrix} = \begin{pmatrix} \cos(\theta) \cos(\zeta) & -r \sin(\theta) \cos(\zeta) & -(R_0 + r \cos(\theta)) \sin(\zeta) \\ \sin(\theta) & r \cos(\theta) & 0 \\ \cos(\theta) \sin(\zeta) & -r \sin(\theta) \sin(\zeta) & (R_0 + r \cos(\theta)) \cos(\zeta) \end{pmatrix},$$

with  $\det(\mathcal{J}) = Rr$ . Thus the transformation Eqn. (A3) is one-to-one and onto for  $r > 0$ .

The unit vectors  $\mathbf{e}_r$ ,  $\mathbf{e}_\theta$ , and  $\mathbf{e}_\zeta$  are computed from the gradient in Cartesian coordinates

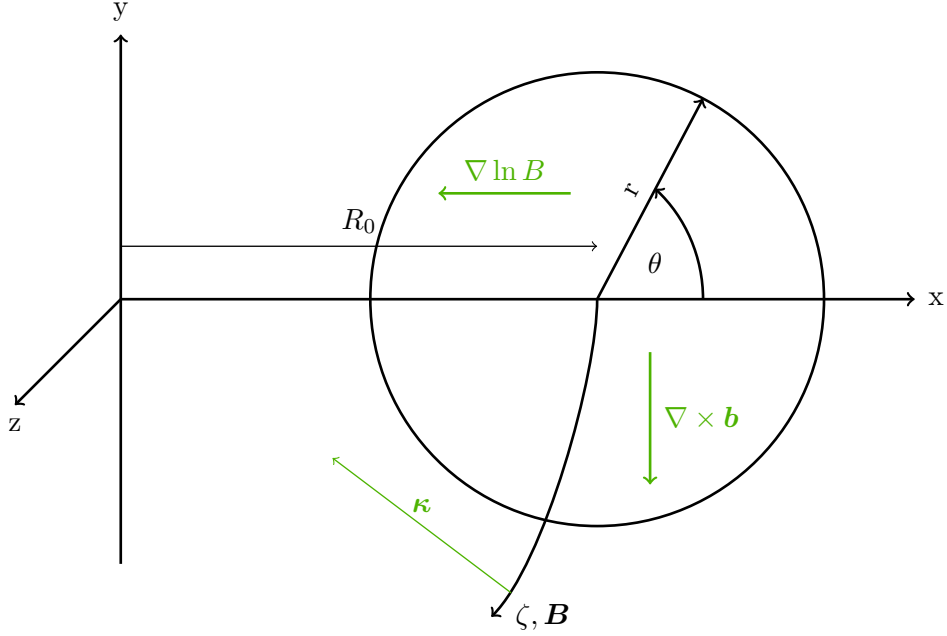


FIG. 53. Simple toroidal coordinates

from Eqn. (A3) as

$$\mathbf{e}_r = \frac{\nabla\theta \times \nabla\zeta}{\nabla r \cdot \nabla\theta \times \nabla\zeta},$$

where  $\mathcal{J} = \nabla r \cdot \nabla\theta \times \nabla\zeta$  and

$$\nabla r = \frac{1}{|\nabla r|} \mathbf{e}_r. \quad (\text{A4})$$

Similar equations hold also for  $\theta$  and  $\zeta$ . Eqn. (A4) relates the unit vectors to the gradients of Eqn. (A3) and defines the scale factor  $h_r = 1/|\nabla r|$ . Similar expressions hold for  $\theta$ , and  $\zeta$  as well. We then evaluate the unit vector in the direction of  $r$ ,  $\theta$ , and  $\zeta$  as

$$\begin{aligned} \mathbf{e}_r &= \cos(\theta) \cos(\zeta) \mathbf{e}_x + \sin(\theta) \mathbf{e}_y + \cos(\theta) \sin(\zeta) \mathbf{e}_z \\ \mathbf{e}_\theta &= -\sin(\theta) \cos(\zeta) \mathbf{e}_z + \cos(\theta) \mathbf{e}_y - \sin(\theta) \sin(\zeta) \mathbf{e}_z \\ \mathbf{e}_\zeta &= \sin(\zeta) \mathbf{e}_x + \cos(\zeta) \mathbf{e}_z. \end{aligned}$$

In this basis, the components of the gradient of a scalar function  $\phi(r, \theta, \zeta)$  are given by

$$\nabla\phi = \frac{\partial\phi}{\partial r} \mathbf{e}_r + \frac{1}{r} \frac{\partial\phi}{\partial\theta} \mathbf{e}_\theta + \frac{1}{R} \frac{\partial\phi}{\partial\zeta} \mathbf{e}_\zeta. \quad (\text{A5})$$

and the components of the curl of a smooth vector field,  $\mathbf{F}$ , are given by

$$(\nabla \times \mathbf{F})_r = \frac{1}{rR} \left( \frac{\partial}{\partial \theta} (RF_\zeta) - \frac{\partial}{\partial \zeta} (rF_\theta) \right) \quad (\text{A6a})$$

$$(\nabla \times \mathbf{F})_\theta = \frac{1}{R} \left( \frac{\partial}{\partial \zeta} F_r - \frac{\partial}{\partial r} (RF_\zeta) \right) \quad (\text{A6b})$$

$$(\nabla \times \mathbf{F})_\zeta = \frac{1}{r} \left( \frac{\partial}{\partial r} (rF_\theta) - \frac{\partial}{\partial \theta} F_r \right). \quad (\text{A6c})$$

Assuming a purely toroidal magnetic field,

$$\mathbf{B} = -\frac{B_0 R_0}{R} \mathbf{e}_\zeta,$$

we find its gradient and curl to be

$$\begin{aligned} \nabla \ln B &= -\frac{1}{R} \mathbf{e}_r \\ \nabla \times \mathbf{b} &= -\frac{1}{R} \sin \theta \mathbf{e}_r - \frac{1}{R} \cos \theta \mathbf{e}_\theta \end{aligned}$$

At the outboard midplane  $\theta$  approximately vanishes, so that these expressions reduce to

$$\nabla \ln B \approx -\frac{1}{R} \mathbf{e}_x \quad (\text{A7})$$

$$\nabla \times \mathbf{b} \approx -\frac{1}{R} \mathbf{e}_y. \quad (\text{A8})$$

Inserting these in the definition of the curvature operator, Eqn. (20), gives

$$\mathcal{K}(u) = -\frac{2}{BR} \frac{\partial u}{\partial y}. \quad (\text{A9})$$

At the outboard midplane, magnetic curvature and the magnetic gradient thus point in the same direction.

---

\* E-mail:ralph.kube@uit.no

- <sup>1</sup> I. H. Hutchinson, R. Boivin, F. Bombarda, P. Bonoli, S. Fairfax, C. Fiore, J. Goetz, S. Golovato, R. Granetz, M. Greenwald, S. Horne, A. Hubbard, J. Irby, B. LaBombard, B. Lipschultz, E. Marmor, G. McCracken, M. Porkolab, J. Rice, J. Snipes, Y. Takase, J. Terry, S. Wolfe, C. Christensen, D. Garnier, M. Graf, T. Hsu, T. Luke, M. May, A. Niemczewski, G. Tinios, J. Schachter, and J. Urbahn, *Physics of Plasmas* **1**, 1511 (1994).
- <sup>2</sup> R. Hazeltine and J. Meiss, *Plasma Confinement*, Dover Books on Physics Series (Dover Publications, 2003).
- <sup>3</sup> J. Freidberg, *Plasma Physics and Fusion Energy* (Cambridge University Press, 2007).
- <sup>4</sup> R. Pitts, R. Buttery, and S. Pinches, *Physics World* **10** (2006).
- <sup>5</sup> P. C. Stangeby, *The Plasma Boundary Of Magnetic Fusion Devices* (IoP Publishing, 2000).
- <sup>6</sup> *Flux Coordinates and Magnetic Field Structure* (Springer Verlag, 1991).
- <sup>7</sup> J. Freidberg, in *Ideal MHD* (Cambridge University Press, 2014) p. 740.
- <sup>8</sup> T. Eich, A. Leonard, R. Pitts, W. Fundamenski, R. Goldston, T. Gray, A. Herrmann, A. Kirk, A. Kallenbach, O. Kardaun, A. Kukushkin, B. LaBombard, R. Maingi, M. Makowski, A. Scarabosio, B. Sieglin, J. Terry, A. Thornton, A. U. Team, and J. E. Contributors, *Nuclear Fusion* **53**, 093031 (2013).
- <sup>9</sup> W. Fundamenski, *Power Exhaust in Fusion Plasmas* (Cambridge University Press, 2010).
- <sup>10</sup> A. J. Wootton, B. A. Carreras, H. Matsumoto, K. McGuire, W. A. Peebles, C. P. Ritz, P. W. Terry, and S. J. Zweben, *Physics of Fluids B: Plasma Physics* **2**, 2879 (1990).
- <sup>11</sup> P. C. Stangeby, *Physics of Plasmas* **9**, 3489 (2002).
- <sup>12</sup> M. V. Umansky, S. I. Krasheninnikov, B. LaBombard, and J. L. Terry, *Physics of Plasmas* **5**, 3373 (1998).
- <sup>13</sup> M. V. Umansky, S. I. Krasheninnikov, B. LaBombard, B. Lipschultz, and J. L. Terry, *Physics of Plasmas* **6**, 2791 (1999).
- <sup>14</sup> B. LaBombard, M. Umansky, R. Boivin, J. Goetz, J. Hughes, B. Lipschultz, D. Mossessian, C. Pitcher, J. Terry, and A. Group, *Nuclear Fusion* **40**, 2041 (2000).
- <sup>15</sup> B. Lipschultz, B. LaBombard, C. S. Pitcher, and R. Boivin, *Plasma Physics and Controlled Fusion* **44**, 733 (2002).

- <sup>16</sup> A. Kallenbach, R. Dux, J. Gafert, G. Haas, L. Horton, M. Jakobi, B. Kurzan, H. Müller, R. Neu, J. Neuhauser, R. Pugno, T. Pütterich, V. Rohde, W. Sandmann, S.-W. Yoon, and the ASDEX Upgrade team, *Nuclear Fusion* **43**, 573 (2003).
- <sup>17</sup> O. E. Garcia, R. A. Pitts, J. Horacek, A. Nielsen, W. Fundamenski, J. Graves, V. Naulin, and J. J. Rasmussen, *Journal of Nuclear Materials* **363-365**, 575 (2007).
- <sup>18</sup> B. LaBombard, R. L. Boivin, M. Greenwald, J. Hughes, B. Lipschultz, D. Mossessian, C. S. Pitcher, J. L. Terry, S. J. Zweben, and the Alcator C-Mod Group, *Physics of Plasmas* **8**, 2107 (2001).
- <sup>19</sup> M. Greenwald, *Plasma Physics and Controlled Fusion* **44**, R27 (2002).
- <sup>20</sup> J. L. Terry, S. J. Zweben, K. Hallatschek, B. LaBombard, R. J. Maqueda, B. Bai, C. J. Boswell, M. Greenwald, D. Kopon, W. M. Nevins, C. S. Pitcher, B. N. Rogers, D. P. Stotler, and X. Q. Xu, *Physics of Plasmas* **10**, 1739 (2003).
- <sup>21</sup> B. LaBombard, J. Rice, A. Hubbard, J. Hughes, M. Greenwald, J. Irby, Y. Lin, B. Lipschultz, E. Marmor, C. Pitcher, N. Smick, S. Wolfe, S. Wukitch, and the Alcator Group, *Nuclear Fusion* **44**, 1047 (2004).
- <sup>22</sup> N. Smick, B. LaBombard, and C. Pitcher, *Journal of Nuclear Materials* **337-339**, 281 (2005).
- <sup>23</sup> G. Kirnev, V. Budaev, S. Grashin, L. Khimchenko, and D. Sarytchev, *Nuclear Fusion* **45**, 459 (2005).
- <sup>24</sup> H. Tanaka, N. Ohno, N. Asakura, Y. Tsuji, H. Kawashima, S. Takamura, Y. Uesugi, and the JT-60U Team, *Nuclear Fusion* **49**, 065017 (2009).
- <sup>25</sup> N. Smick, B. LaBombard, and I. Hutchinson, *Nuclear Fusion* **53**, 023001 (2013).
- <sup>26</sup> P. Helander and D. J. Sigmar, *Collisional Transport in Magnetized Plasmas* (Cambridge University Press, 2002).
- <sup>27</sup> A. Chankin, *Journal of Nuclear Materials* **241-243**, 199 (1997).
- <sup>28</sup> R. Pitts, J. Horacek, W. Fundamenski, O. Garcia, A. Nielsen, M. Wischmeier, V. Naulin, and J. J. Rasmussen, *Journal of Nuclear Materials* **363-365**, 505 (2007), plasma-Surface Interactions-17.
- <sup>29</sup> S. K. Erents, A. V. Chankin, G. F. Matthews, and P. C. Stangeby, *Plasma Physics and Controlled Fusion* **42**, 905 (2000).
- <sup>30</sup> C. Hidalgo, B. Goncalves, C. Silva, M. A. Pedrosa, K. Erents, M. Hron, and G. F. Matthews, *Phys. Rev. Lett.* **91**, 065001 (2003).

- <sup>31</sup> R. Pitts, G. Vayakis, G. Matthews, and V. Vershkov, *Journal of Nuclear Materials* **176–177**, 893 (1990).
- <sup>32</sup> N. Asakura, S. Sakurai, N. Hosogane, M. Shimada, K. Itami, Y. Koide, and O. Naito, *Nuclear Fusion* **39**, 1983 (1999).
- <sup>33</sup> N. Asakura, S. Sakurai, M. Shimada, Y. Koide, N. Hosogane, and K. Itami, *Phys. Rev. Lett.* **84**, 3093 (2000).
- <sup>34</sup> A. Chankin, G. Corrigan, S. Erents, G. Matthews, J. Spence, and P. Stangeby, *Journal of Nuclear Materials* **290–293**, 518 (2001).
- <sup>35</sup> A. Chankin and P. Stangeby, *Nuclear Fusion* **41**, 421 (2001).
- <sup>36</sup> M. Endler, *Journal of Nuclear Materials* **266–269**, 84 (1999).
- <sup>37</sup> A. V. Nedospasov, *Soviet Journal of Plasma Physics* **15**, 659 (1989).
- <sup>38</sup> X. Garbet, L. Laurent, J.-P. Roubin, and A. Samain, *Nuclear Fusion* **31**, 967 (1991).
- <sup>39</sup> M. Endler, H. Niedermeyer, L. Giannone, E. Kolzhauer, A. Rudyj, G. Theimer, and N. Tsois, *Nuclear Fusion* **35**, 1307 (1995).
- <sup>40</sup> T. T. Ribeiro and B. Scott, *Plasma Physics and Controlled Fusion* **47**, 1657 (2005).
- <sup>41</sup> T. Ribeiro, *Turbulence Studies in the Scrape-off Layer of Tokamak Plasma by Three-dimensional Gyrofluid Simulations*, Ph.D. thesis, Universidade Tecnica de Lisboa (2005).
- <sup>42</sup> B. Lipschultz, B. Labombard, J. L. Terry, C. Boswell, and I. H. Hutchinson, *Divertor Physics Research on Alcator C-Mod*, Tech. Rep. (Plasma Science and Fusion Center, MIT, 2005).
- <sup>43</sup> K. McCormick, G. Kyriakakis, J. Neuhauser, E. Kakoulidis, J. Schweinzer, and N. Tsois, *Journal of Nuclear Materials* **196–198**, 264 (1992), plasma-Surface Interactions in Controlled Fusion Devices Proceedings of the Tenth International Conference on Plasma-Surface Interactions in Controlled Fusion Devices.
- <sup>44</sup> B. Labombard, J. Goetz, I. Hutchinson, D. Jablonski, J. Kesner, C. Kurz, B. Lipschultz, G. McCracken, A. Niemczewski, J. Terry, A. Allen, R. Boivin, F. Bombarda, P. Bonoli, C. Christensen, C. Fiore, D. Garnier, S. Golovato, R. Granetz, M. Greenwald, S. Horne, A. Hubbard, J. Irby, D. Lo, D. Lumma, E. Marmor, M. May, A. Mazurenko, R. Nachtrieb, H. Ohkawa, P. O’Shea, M. Porkolab, J. Reardon, J. Rice, J. Rost, J. Schachter, J. Snipes, J. Sorci, P. Stek, Y. Takase, Y. Wang, R. Watterson, J. Weaver, B. Welch, and S. Wolfe, *Journal of Nuclear Materials* **241–243**, 149 (1997).

- <sup>45</sup> J. Connor, G. Counsell, S. Erents, S. Fielding, B. LaBombard, and K. Morel, *Nuclear Fusion* **39**, 169 (1999).
- <sup>46</sup> B. Lipschultz, D. Whyte, and B. LaBombard, *Plasma Physics and Controlled Fusion* **47**, 1559 (2005).
- <sup>47</sup> V. Naulin, *Journal of Nuclear Materials* **363–365**, 24 (2007).
- <sup>48</sup> O. E. Garcia, V. Naulin, A. H. Nielsen, and J. J. Rasmussen, *Phys. Rev. Lett.* **92**, 165003 (2004).
- <sup>49</sup> O. E. Garcia, N. H. Bian, V. Naulin, A. H. Nielsen, and J. J. Rasmussen, *Physics of Plasmas* **12**, 090701 (2005).
- <sup>50</sup> O. E. Garcia, N. H. Bian, V. Naulin, A. H. Nielsen, and J. J. Rasmussen, *Physica Scripta* **2006**, 104 (2006).
- <sup>51</sup> O. Garcia, J. Horacek, R. Pitts, A. Nielsen, W. Fundamenski, V. Naulin, and J. J. Rasmussen, *Nuclear Fusion* **47**, 667 (2007).
- <sup>52</sup> D. A. D'Ippolito, J. R. Myra, and S. J. Zweben, *Physics of Plasmas* **18**, 060501 (2011).
- <sup>53</sup> S. J. Zweben, *Physics of Fluids* **28**, 974 (1985).
- <sup>54</sup> G. Y. Antar, S. I. Krasheninnikov, P. Devynck, R. P. Doerner, E. M. Hollmann, J. A. Boedo, S. C. Luckhardt, and R. W. Conn, *Phys. Rev. Lett.* **87**, 065001 (2001).
- <sup>55</sup> J. A. Boedo, D. Rudakov, R. Moyer, S. Krasheninnikov, D. Whyte, G. McKee, G. Tynan, M. Schaffer, P. Stangeby, P. West, S. Allen, T. Evans, R. Fonck, E. Hollmann, A. Leonard, A. Mahdavi, G. Porter, M. Tillack, and G. Antar, *Physics of Plasmas* **8**, 4826 (2001).
- <sup>56</sup> D. L. Rudakov, J. A. Boedo, R. A. Moyer, S. Krasheninnikov, A. W. Leonard, M. A. Mahdavi, G. R. McKee, G. D. Porter, P. C. Stangeby, J. G. Watkins, W. P. West, D. G. Whyte, and G. Antar, *Plasma Physics and Controlled Fusion* **44**, 717 (2002).
- <sup>57</sup> G. Y. Antar, G. Counsell, Y. Yu, B. Labombard, and P. Devynck, *Physics of Plasmas* **10**, 419 (2003).
- <sup>58</sup> J. A. Boedo, D. L. Rudakov, R. A. Moyer, G. R. McKee, R. J. Colchin, M. J. Schaffer, P. G. Stangeby, W. P. West, S. L. Allen, T. E. Evans, R. J. Fonck, E. M. Hollmann, S. Krasheninnikov, A. W. Leonard, W. Nevins, M. A. Mahdavi, G. D. Porter, G. R. Tynan, D. G. Whyte, and X. Xu, *Physics of Plasmas* **10**, 1670 (2003).
- <sup>59</sup> G. S. Kirnev, V. P. Budaev, S. A. Grashin, E. V. Gerasimov, and L. N. Khimchenko, *Plasma Physics and Controlled Fusion* **46**, 621 (2004).

- <sup>60</sup> S. J. Zweben, J. A. Boedo, O. Grulke, C. Hidalgo, B. LaBombard, R. J. Maqueda, P. Scarin, and J. L. Terry, *Plasma Physics and Controlled Fusion* **49**, S1 (2007).
- <sup>61</sup> H. Johnsen, H. L. Pécseli, and J. Trulsen, *Physics of Fluids* **30**, 2239 (1987).
- <sup>62</sup> F. J. Øynes, H. L. Pecseli, and K. Rypdal, *Phys. Rev. Lett.* **75**, 81 (1995).
- <sup>63</sup> G. Y. Antar, P. Devynck, X. Garbet, and S. C. Luckhardt, *Physics of Plasmas* **8**, 1612 (2001).
- <sup>64</sup> O. Grulke, J. L. Terry, B. LaBombard, and S. J. Zweben, *Physics of Plasmas* **13**, 012306 (2006).
- <sup>65</sup> O. Grulke, J. L. Terry, I. Cziegler, B. LaBombard, and O. E. Garcia, *Nuclear Fusion* **54**, 043012 (2014).
- <sup>66</sup> J. Terry, S. Zweben, O. Grulke, M. Greenwald, and B. LaBombard, *Journal of Nuclear Materials* **337–339**, 322 (2005).
- <sup>67</sup> M. Agostini, J. Terry, P. Scarin, and S. Zweben, *Nuclear Fusion* **51**, 053020 (2011).
- <sup>68</sup> I. Cziegler, *Turbulence and Transport Phenomena in Edge and Scrape-Off-Layer Plasmas*, Ph.D. thesis, Massachusetts Institute of Technology (2011).
- <sup>69</sup> S. I. Krasheninnikov, *Physics Letters A* **283**, 368 (2001).
- <sup>70</sup> D. A. D'Ippolito, J. R. Myra, and S. I. Krasheninnikov, *Physics of Plasmas* **9**, 222 (2002).
- <sup>71</sup> O. E. Garcia, N. H. Bian, and W. Fundamenski, *Physics of Plasmas* **13**, 082309 (2006).
- <sup>72</sup> O. Garcia, *Plasma and Fusion Research: Review Articles* **4** (2009).
- <sup>73</sup> N. Bian, S. Benkadda, J.-V. Paulsen, and O. E. Garcia, *Physics of Plasmas* **10**, 671 (2003).
- <sup>74</sup> S. I. Krasheninnikov, D. A. D'Ippolito, and J. R. Myra, *Journal of Plasma Physics* **74**, 679 (2008).
- <sup>75</sup> D. A. Russell, D. A. D'Ippolito, J. R. Myra, W. M. Nevins, and X. Q. Xu, *Phys. Rev. Lett.* **93**, 265001 (2004).
- <sup>76</sup> S. Krasheninnikov, D. Rutovi, and Y. Guanghai, *Journal of Plasma Fusion Research Series* **6**, 139 (2004).
- <sup>77</sup> D. D. Ryutov and R. H. Cohen, *Contributions to Plasma Physics* **44**, 168 (2004).
- <sup>78</sup> J. R. Myra and D. A. D'Ippolito, *Physics of Plasmas* **12**, 092511 (2005).
- <sup>79</sup> J. R. Myra, D. A. Russell, and D. A. D'Ippolito, *Physics of Plasmas* **13**, 112502 (2006).
- <sup>80</sup> G. Q. Yu, S. I. Krasheninnikov, and P. N. Guzdar, *Physics of Plasmas* **13**, 042508 (2006).
- <sup>81</sup> B. Scott, *Contributions to Plasma Physics* **38**, 171 (1998).
- <sup>82</sup> B. D. Scott, *New Journal of Physics* **7**, 92 (2005).

- <sup>83</sup> B. D. Scott, *Plasma Physics and Controlled Fusion* **49**, S25 (2007).
- <sup>84</sup> P. Manz, D. Carralero, G. Birkenmeier, H. W. Müller, S. H. Müller, G. Fuchert, B. D. Scott, and U. Stroth, *Physics of Plasmas* **20**, 102307 (2013).
- <sup>85</sup> C. Theiler, A. Diallo, A. Fasoli, I. Furno, B. Labit, M. Podestà, F. M. Poli, and P. Ricci, *Physics of Plasmas* **15**, 042303 (2008).
- <sup>86</sup> I. Furno, C. Theiler, D. Lançon, A. Fasoli, D. Iraji, P. Ricci, M. Spolaore, and N. Vianello, *Plasma Physics and Controlled Fusion* **53**, 124016 (2011).
- <sup>87</sup> I. Furno, M. Spolaore, C. Theiler, N. Vianello, R. Cavazzana, and A. Fasoli, *Phys. Rev. Lett.* **106**, 245001 (2011).
- <sup>88</sup> G. Birkenmeier, F. M. Laggner, M. Willensdorfer, T. Kobayashi, P. Manz, E. Wolfrum, D. Carralero, R. Fischer, B. Sieglin, G. Fuchert, U. Stroth, and the ASDEX upgrade team, *Plasma Physics and Controlled Fusion* **56**, 075019 (2014).
- <sup>89</sup> N. Katz, J. Egedal, W. Fox, A. Le, and M. Porkolab, *Phys. Rev. Lett.* **101**, 015003 (2008).
- <sup>90</sup> R. Monk and the JET Team, *Nuclear Fusion* **39**, 1751 (1999).
- <sup>91</sup> A. Loarte, *Plasma Physics and Controlled Fusion* **43**, R183 (2001).
- <sup>92</sup> J. Myra, W. Davis, D. D'Ippolito, B. LaBombard, D. Russell, J. Terry, and S. Zweben, *Nuclear Fusion* **53**, 073013 (2013).
- <sup>93</sup> I. H. Hutchinson, *Principles of Plasma Diagnostics*, edited by S. edition (Cambridge University Press, 2002).
- <sup>94</sup> O. E. Garcia, *Phys. Rev. Lett.* **108**, 265001 (2012).
- <sup>95</sup> J. Terry, N. Basse, I. Cziegler, M. Greenwald, O. Grulke, B. LaBombard, S. Zweben, E. Edlund, J. Hughes, L. Lin, Y. Lin, M. Porkolab, M. Sampsell, B. Veto, and S. Wukitch, *Nuclear Fusion* **45**, 1321 (2005).
- <sup>96</sup> S. J. Zweben and S. S. Medley, *Physics of Fluids B: Plasma Physics (1989-1993)* **1**, 2058 (1989).
- <sup>97</sup> R. J. Maqueda, G. A. Wurden, S. Zweben, L. Roquemore, H. Kugel, D. Johnson, S. Kaye, S. Sabbagh, and R. Maingi, *Review of Scientific Instruments* **72**, 931 (2001).
- <sup>98</sup> J. L. Terry, S. J. Zweben, B. Bose, O. Grulke, E. S. Marmor, J. Lowrance, V. Mastrocola, and G. Renda, *Review of Scientific Instruments* **75**, 4196 (2004).
- <sup>99</sup> D. Stotler, B. LaBombard, J. Terry, and S. Zweben, *Journal of Nuclear Materials* **313–316**, 1066 (2003), *plasma-Surface Interactions in Controlled Fusion Devices* 15.

- <sup>100</sup> D. Stotler, J. Boedo, B. LeBlanc, R. Maqueda, and S. Zweben, *Journal of Nuclear Materials* **363–365**, 686 (2007), [jce:titlejPlasma-Surface Interactions-17j/ce:titlej](#).
- <sup>101</sup> S. J. Zweben, D. P. Stotler, J. L. Terry, B. LaBombard, M. Greenwald, M. Muterspaugh, C. S. Pitcher, A. C.-M. Group, K. Hallatschek, R. J. Maqueda, B. Rogers, J. L. Lowrance, V. J. Mastrocola, and G. F. Renda, *Physics of Plasmas* **9**, 1981 (2002).
- <sup>102</sup> N. Bisai, A. Das, S. Deshpande, R. Jha, P. Kaw, A. Sen, and R. Singh, *Physics of Plasmas* **12**, 072520 (2005).
- <sup>103</sup> J. R. Myra, D. A. D’Ippolito, D. P. Stotler, S. J. Zweben, B. P. LeBlanc, J. E. Menard, R. J. Maqueda, and J. Boedo, *Physics of Plasmas* **13**, 092509 (2006).
- <sup>104</sup> D. A. Russell, J. R. Myra, and D. A. D’Ippolito, *Physics of Plasmas* **14**, 102307 (2007).
- <sup>105</sup> D. A. Russell, J. R. Myra, and D. A. D’Ippolito, *Physics of Plasmas* **16**, 122304 (2009).
- <sup>106</sup> M. Agostini, S. J. Zweben, R. Cavazzana, P. Scarin, G. Serianni, R. J. Maqueda, and D. P. Stotler, *Physics of Plasmas* **14**, 102305 (2007).
- <sup>107</sup> S. H. Müller, A. Diallo, A. Fasoli, I. Furno, B. Labit, and M. Podestà, *Physics of Plasmas* **14**, 110704 (2007).
- <sup>108</sup> I. Furno, B. Labit, M. Podestà, A. Fasoli, S. H. Müller, F. M. Poli, P. Ricci, C. Theiler, S. Brunner, A. Diallo, and J. Graves, *Phys. Rev. Lett.* **100**, 055004 (2008).
- <sup>109</sup> I. Furno, B. Labit, A. Fasoli, F. M. Poli, P. Ricci, C. Theiler, S. Brunner, A. Diallo, J. P. Graves, M. Podestà, and S. H. Müller, *Physics of Plasmas* **15**, 055903 (2008).
- <sup>110</sup> T. Happel, F. Greiner, N. Mahdizadeh, B. Nold, M. Ramisch, and U. Stroth, *Phys. Rev. Lett.* **102**, 255001 (2009).
- <sup>111</sup> G. Fuchert, G. Birkenmeier, B. Nold, M. Ramisch, and U. Stroth, *Plasma Physics and Controlled Fusion* **55**, 125002 (2013).
- <sup>112</sup> S. I. Krasheninnikov and A. I. Smolyakov, *Physics of Plasmas* **14**, 102503 (2007).
- <sup>113</sup> S. I. Krasheninnikov and A. I. Smolyakov, *Physics of Plasmas* **15**, 055909 (2008).
- <sup>114</sup> N. Bisai, A. Das, S. Deshpande, R. Jha, P. Kaw, A. Sen, and R. Singh, *Physics of Plasmas* **12**, 102515 (2005).
- <sup>115</sup> H. L. Pecseli, *Fluctuations in Physical systems*, Vol. 1 (Cambridge University Press, 2000).
- <sup>116</sup> R. Fitzpatrick, *Plasma Physics: An Introduction* (CRC Press, Taylor and Francis Group, 2014).

- <sup>117</sup> S. Chapman and T. Cowling, *The Mathematical Theory of Non-uniform gases* (Cambridge University Press, 1970).
- <sup>118</sup> S. I. Braginskii, *Review of Plasma Physics* **1**, 205 (1965).
- <sup>119</sup> O. E. Garcia, “Lecture notes on plasma physics,” (2012).
- <sup>120</sup> D. A. D’Ippolito and J. R. Myra, *Physics of Plasmas* **10**, 4029 (2003).
- <sup>121</sup> J. R. Myra, D. A. D’Ippolito, S. I. Krasheninnikov, and G. Q. Yu, *Physics of Plasmas* **11**, 4267 (2004).
- <sup>122</sup> The Boussinesq approximation consists of neglecting particle density variations, except when multiplied by the effective gravity of the system at hand. It is valid in the case where  $|\nabla n| \ll n$ . For seeded blob simulations however,  $|\nabla n| \gg n$  may be true. Nevertheless, most work on seeded blob simulations neglects this term. Numerical simulations studying the effect of the Boussinesq approximation on the radial propagation of seeded blobs have shown, that including the full inertia term causes a faster radial advection of the blobs [80].
- <sup>123</sup> O. E. Garcia, *Convection and shear flows in fluids and magnetized plasmas*, Ph.D. thesis, University of Tromsø (2002).
- <sup>124</sup> Y. H. Xu, S. Jachmich, R. R. Weynants, and the TEXTOR team, *Plasma Physics and Controlled Fusion* **47**, 1841 (2005).
- <sup>125</sup> J. M. Dewhurst, B. Hnat, N. Ohno, R. O. Dendy, S. Masuzaki, T. Morisaki, and A. Komori, *Plasma Physics and Controlled Fusion* **50**, 095013 (2008).
- <sup>126</sup> G. Xu, V. Naulin, W. Fundamenski, C. Hidalgo, J. Alonso, C. Silva, B. Gonçalves, A. Nielsen, J. J. Rasmussen, S. Krasheninnikov, B. Wan, M. Stamp, and J. E. Contributors, *Nuclear Fusion* **49**, 092002 (2009).
- <sup>127</sup> J. Cheng, L. W. Yan, W. Y. Hong, K. J. Zhao, T. Lan, J. Qian, A. D. Liu, H. L. Zhao, Y. Liu, Q. W. Yang, J. Q. Dong, X. R. Duan, and Y. Liu, *Plasma Physics and Controlled Fusion* **52**, 055003 (2010).
- <sup>128</sup> B. Nold, G. D. Conway, T. Happel, H. W. Müller, M. Ramisch, V. Rohde, U. Stroth, and the ASDEX Upgrade Team, *Plasma Physics and Controlled Fusion* **52**, 065005 (2010).
- <sup>129</sup> J. R. Myra, D. A. Russell, and D. A. D’Ippolito, *Physics of Plasmas* **15**, 032304 (2008).
- <sup>130</sup> K. P. Balanda and H. L. MacGillivray, *The American Statistician* **42**, pp. 111 (1988).
- <sup>131</sup> J. P. Graves, J. Horacek, R. A. Pitts, and K. I. Hopcraft, *Plasma Physics and Controlled Fusion* **47**, L1 (2005).

- <sup>132</sup> F. Sattin, P. Scarin, M. Agostini, R. Cavazzana, G. Serianni, M. Spolaore, and N. Vianello, *Plasma Physics and Controlled Fusion* **48**, 1033 (2006).
- <sup>133</sup> B. Labit, I. Furno, A. Fasoli, A. Diallo, S. H. Müller, G. Plyushchev, M. Podestà, and F. M. Poli, *Phys. Rev. Lett.* **98**, 255002 (2007).
- <sup>134</sup> O. E. Garcia, S. M. Fritzner, R. Kube, I. Cziegler, B. LaBombard, and J. L. Terry, *Phys. Plasmas* **20**, 055901 (2013).
- <sup>135</sup> O. E. Garcia, J. Horacek, R. A. Pitts, A. H. Nielsen, W. Fundamenski, J. P. Graves, V. Naulin, and J. J. Rasmussen, *Plasma Physics and Controlled Fusion* **48**, L1 (2006).
- <sup>136</sup> F. Sattin, N. Vianello, and M. Valisa, *Physics of Plasmas* **11**, 5032 (2004).
- <sup>137</sup> D. Rudakov, J. Boedo, R. Moyer, P. Stangeby, J. Watkins, D. Whyte, L. Zeng, N. Brooks, R. Doerner, T. Evans, M. Fenstermacher, M. Groth, E. Hollmann, S. Krasheninnikov, C. Lasnier, A. Leonard, M. Mahdavi, G. McKee, A. McLean, A. Pigarov, W. Wampler, G. Wang, W. West, and C. Wong, *Nuclear Fusion* **45**, 1589 (2005).
- <sup>138</sup> W. Fundamenski, O. Garcia, V. Naulin, R. Pitts, A. Nielsen, J. J. Rasmussen, J. Horacek, J. Graves, and J. E. contributors, *Nuclear Fusion* **47**, 417 (2007).
- <sup>139</sup> R. Cohen, B. LaBombard, D. Ryutov, J. L. Terry, M. Umansky, X. Xu, and S. Zweben, *Nuclear Fusion* **47**, 612 (2007).
- <sup>140</sup> C. Theiler, I. Furno, P. Ricci, A. Fasoli, B. Labit, S. H. Müller, and G. Plyushchev, *Phys. Rev. Lett.* **103**, 065001 (2009).
- <sup>141</sup> R. Kube and O. E. Garcia, *Physics of Plasmas* **18**, 102314 (2011).
- <sup>142</sup> R. Kube and O. E. Garcia, *Physics of Plasmas* **19**, (2012).
- <sup>143</sup> B. P. van Milligen, R. Sánchez, B. A. Carreras, V. E. Lynch, B. LaBombard, M. A. Pedrosa, C. Hidalgo, B. Gonçalves, R. Balbín, and T. W.-A. Team, *Physics of Plasmas* **12**, 052507 (2005).
- <sup>144</sup> P. Devynck, J. Brotankova, P. Peleman, M. Spolaore, H. Figueiredo, M. Hron, G. Kirnev, E. Martines, J. Stockel, G. Van Oost, and V. Weinzettl, *Physics of Plasmas* **13**, 102505 (2006).
- <sup>145</sup> T. A. Carter, *Physics of Plasmas* **13**, 010701 (2006).
- <sup>146</sup> J. Rice, *Advances in Applied Probability* **9**, pp. 553 (1977).
- <sup>147</sup> H. L. Pécseli and J. Trulsen, *Physics of Fluids B: Plasma Physics (1989-1993)* **1**, 1616 (1989).

- <sup>148</sup> L. Lao, H. S. John, R. Stambaugh, A. Kellman, and W. Pfeiffer, *Nuclear Fusion* **25**, 1611 (1985).
- <sup>149</sup> R. S. Granetz, I. H. Hutchinson, J. Gerolamo, W. Pina, and C. Tsui, *Review of Scientific Instruments* **61**, 2967 (1990).
- <sup>150</sup> N. Smick and B. LaBombard, *Review of Scientific Instruments* **80**, 023502 (2009).
- <sup>151</sup> R. Fraile and E. García-Ortega, *Journal of Applied Meteorology*, *Journal of Applied Meteorology* **44**, 1620 (2005).
- <sup>152</sup> B. LaBombard, J. Goetz, C. Kurz, D. Jablonski, B. Lipschultz, G. McCracken, A. Niemczewski, R. L. Boivin, F. Bombarda, C. Christensen, S. Fairfax, C. Fiore, D. Garnier, M. Graf, S. Golovato, R. Granetz, M. Greenwald, S. Horne, A. Hubbard, I. Hutchinson, J. Irby, J. Kesner, T. Luke, E. Marmar, M. May, P. O'Shea, M. Porkolab, J. Reardon, J. Rice, J. Schachter, J. Snipes, P. Stek, Y. Takase, J. Terry, G. Tinios, R. Watterson, B. Welch, and S. Wolfe, *Physics of Plasmas* **2**, 2242 (1995).
- <sup>153</sup> R. Kube, O. Garcia, B. LaBombard, J. Terry, and S. Zweben, *Journal of Nuclear Materials* **438, Supplement**, S505 (2013), proceedings of the 20th International Conference on Plasma-Surface Interactions in Controlled Fusion Devices.
- <sup>154</sup> D. Brunner, B. LaBombard, R. M. Churchill, J. Hughes, B. Lipschultz, R. Ochoukov, T. D. Rognlien, C. Theiler, J. Walk, M. V. Umansky, and D. Whyte, *Plasma Physics and Controlled Fusion* **55**, 095010 (2013).
- <sup>155</sup> J. Madsen, O. E. Garcia, J. Stærk Larsen, V. Naulin, A. H. Nielsen, and J. J. Rasmussen, *Physics of Plasmas* **18**, 112504 (2011).
- <sup>156</sup> M. Wiesenberger, J. Madsen, and A. Kendl, *Physics of Plasmas* **21**, 092301 (2014).
- <sup>157</sup> B. Labombard and L. Lyons, *Review of Scientific Instruments* **78**, 073501 (2007).